

A procedure to analyze nonlinear density waves in Saturn's rings using several occultation profiles

Nicole J. Rappaport^{*,1}, Pierre-Yves Longaretti^{2,3}, Richard G. French⁴, Essam A. Marouf⁵, and Colleen A. McGhee⁴

¹ Jet Propulsion Laboratory, California Institute of Technology, m.s. 301-150, 4800 Oak Grove Drive, Pasadena CA 91109

² Université Joseph Fourier, Laboratoire d'Astrophysique de Grenoble, BP 53, 38041 Grenoble Cedex 9 FRANCE

³ Centre National de la Recherche Scientifique (CNRS) / INSU

⁴ Astronomy Department, Wellesley College, Wellesley, MA 02181

⁵ San Jose State University, One Washington Square, San Jose, CA 95192

* Corresponding author e-mail address: Nicole.J.Rappaport@jpl.nasa.gov

Revision: 16

Pages: 50

Tables: 2

Figures: 13

Proposed running head: Density Wave Analysis

Editorial correspondence to: Dr Nicole J. Rappaport

Jet Propulsion Laboratory

Mail Stop 301-150

4800 Oak Grove Drive

Pasadena, California 91109

Phone: 818 354 8211

Fax: 818 393 7116

E-mail address: Nicole.J.Rappaport@jpl.nasa.gov

ABSTRACT

Cassini radio science experiments have provided multiple occultation optical depth profiles of Saturn's rings that can be used in combination to analyze density waves. This paper establishes an accurate procedure of inversion of the wave profiles to reconstruct the wave kinematic parameters as a function of semi-major axis, in the nonlinear regime. This procedure is established using simulated data in the presence of realistic noise perturbations, to control the reconstruction error. It is then applied to the Mimas 5:3 density wave.

There are two important concepts at the basis of this procedure. The first one is that it uses the nonlinear representation of density waves, and the second one is that it relies on a combination of optical depth profiles instead of just one profile. A related method to analyze density waves was devised by Longaretti and Borderies (1986) to study the nonlinear density wave associated with the Mimas 5:3 resonance, but the single photopolarimetric profile provided limited constraints. Other studies of density waves analyzing Cassini data (Colwell and Esposito 2007; Tiscareno et al. 2007) are based on the linear theory and find inconsistent results from profile to profile. Multiple cuts of the rings are helpful in a fundamental way to ensure the accuracy of the procedure by forcing consistency among the various optical depth profiles.

By way of illustration we have applied our procedure to the Mimas 5:3 density wave. We were able to recover precisely the kinematic parameters from the radio experiment occultation data in most of the propagation region; a preliminary analysis of the pressure-corrected dispersion allowed us to determine new but still uncertain values for the opacity ($K \simeq 0.02 \text{ cm}^2/\text{g}$) and velocity dispersion of ($c_o \simeq 0.6 \text{ cm/s}$) in the wave region.

Our procedure constitutes the first step in our planned analysis of the density waves of Saturn's rings. It is very accurate and efficient in the far-wave region. However, improvements are required within the first wavelength. The ways in which this method can be used to establish diagnostics of ring physics are outlined.

Key Words: Saturn's rings, nonlinear density waves

1 Introduction

The wealth of new data provided by the Cassini mission (and in particular, the collection of independent radial wave optical depth profiles of Saturn's rings) opens the possibility to use wave dynamics to establish physical diagnostics of ring physics to a level of accuracy substantially higher than what was possible with Voyager. However, such a research program requires an accurate determination of the wave kinematic parameters throughout the wave propagation region. This has prompted us to reinvestigate this last problem.

Many density waves in Saturn's rings are strong and nonlinear – that is they cannot be modeled by the linear theory of density waves fully described e.g. by Shu (1984) – but this linear theory is nevertheless used due to the absence of a well-established nonlinear inversion procedure (e.g., Nicholson et al. 1990; Rosen et al. 1991a,b; Spilker et al. 2004; Tiscareno et al. 2006, 2007). This paper presents a new approach to analyze linear and nonlinear density waves. The procedure is established through the use of a number of simulated optical depth profiles, as only simulated data allow us to compare the reconstructed kinematic parameters with the original ones. It is applied next to the Mimas 5:3 density wave as observed by the Cassini Radio Science occultation experiment, as an example. This procedure will serve as the basis of several subsequent studies of real data. The approach adopted here considerably sharpens the method described by Longaretti and Borderies (1986), which extracted the maximum information from one Voyager photopolarimeter stellar occultation profile. However, one profile is insufficient to accurately constrain all the parameters of the model to the level of accuracy required to produce new and detailed diagnostics of the ring physics.

There are several motivations for analyzing density waves, and especially nonlinear density waves. The first objective of determining the kinematic behavior of ring density waves is to test the background kinematic model described in section 2, as possible systematic deviations from this model might provide information on physics that are yet unknown or not well constrained. Cassini provides many different radio occultation profiles of the rings, which can be used to verify that a single set of wave parameters can be determined for various observations of a wave at various longitudes with respect to that of the associated satellite (at least when modulations due to satellite orbital variations or other physical effects are weak enough).

For each wave, the set of kinematic parameters determined by the method described in this paper, coupled to the analysis of the evanescent part of the wave (which may require extraneous dynamical constraints to be accomplished), form the basis of the next objective, which is to measure as precisely as possible the torques exerted by the satellites on the rings. Such a direct measurement was previously attempted in Longaretti and Borderies (1986), but with limited success due to insufficient constraints in the first wavelength of the studied wave, and to failure of the WKBJ approximation in the vicinity of the resonance. This type of torque measurement based on a determination of the wave kinematics can only be performed in Saturn's rings, and therefore constitutes a unique way to verify the dynamical theoretical predictions for such torques. The measurement and verification of the torque are directly relevant to the dynamics of disk-satellite interactions in general. The extent to which dynamical constraints are required on top of a purely kinematic description of the wave remains to be seen; this bears on the model dependence of such

a torque measurement.

Another important study that will follow from this paper is the detailed analysis of the ring stress tensor, with the hope that this may in turn provide useful constraints on the ring particles collisional properties. We wish to identify statistically the various stress behaviors that might be found, depending, for instance on the ring region or ring background optical depth. Several models of damping exist. For instance, Borderies et al. (1983) and Shu et al. (1985a) predict a bimodal behavior as a function of the ring mean optical depth in dilute rings. Borderies et al. (1985) generated models for dense rings. This research program requires combining the kinematic reconstruction method developed here with the nonlinear (pressure-corrected) dispersion relation and at least one generic dynamical equation describing wave propagation and damping (such as the ones derived in Shu et al. 1985a or Borderies et al. 1986).

In the bulk of this paper, we simulate a density wave that has some similarities with the Mimas 5:3 density wave, as observed in eight diffraction-corrected Cassini radio occultation profiles. We did not try to simulate this wave precisely, because the purpose of the simulation was to establish the procedure. A preliminary and simplified analysis of real data pertaining to this wave is presented in section 5. The reader might wonder why we started with simulated data. The reason is that such an analysis is in itself already very complex and it is important to separate this complexity from that inherent to the analysis of real data. There are several reasons for which the analysis of simulated data is difficult.

The first reason is the nonlinearity in itself. The equation describing the shape of the wave, with its large troughs and narrow peaks, does not provide a model that one can readily fit to the data. The fit turns out to be extremely sensitive to the dependence of the wave phase on semi-major axis, and so the procedure must allow for a very precise determination of this quantity. By using simulated data, we can compare how the reconstructed wave kinematic parameters such as the wave phase compare to the ones used in constructing the data; we can therefore quantify the error in the reconstruction method developed here.

The next difficulty is associated with the fact that the absolute radial scale of Saturn's rings is presently known to only ± 2 km (Nicholson et al. 1990; French et al. 1993; Jacobson et al. 2006). Long period variations in the satellite's orbit may produce similar radial shifts in the resonance location, and are expected to produce variations in the wave propagation which are not yet modeled. The uncertainty in the radial scale, at least, will be reduced by future kinematic models to the level of about 100 m.

Another major problem comes from the fact that one must distinguish between radius r and semi-major axis a ; the relation $r = a [1 - e \cos(m\phi + m\Delta)]$ (see section 2 for definitions of the variables and discussion of this relation) is simple only superficially.

Other effects add their own complexity to the data. Interestingly, the noise present in real data (which we took into account in our simulations) is not a real problem, although the need for several profiles to constrain a unique self-consistent solution results mostly from the presence of noise. However, and as indicated by the work of Lewis and Stewart (2000, 2005), gravitational clustering can cause significant effects on the structure of local density maxima. Also, the gravitational wakes observed in the rings (see for instance Hedman et al. 2007; Colwell et al. 2006, 2007) make it necessary to normalize the background optical depth among the various profiles, and may affect

the optical depth profile of the wave in an as yet uncontrolled way. Focusing on simulated data allows us to ignore this added complexity in the first step .

Before describing our procedure in section 4, we begin in section 2 by gathering the basic equations of the theoretical streamline kinematic model. Section 3 describes and illustrates the method to obtain the simulated data. Section 5 applies the procedure to the Mimas 5:3 density wave. Section 6 summarizes and concludes the paper with a discussion of future work.

2 Theoretical Model

The most striking observed characteristic of density waves – the shape of the peaks and troughs – is kinematic in nature. Dynamics enters mostly through the nonlinear dispersion relation, which specifies the change of the wavelength with radius as the wave propagates, and through the control of the wave amplitude; another dynamical feature is the existence of an evanescent zone. More generally, dynamics controls the way the observed kinematic features are spatially modulated. It is therefore legitimate first to focus on the information that can be recovered from kinematic constraints, relying as little as possible on dynamical ones.

The major difficulty of this program lies in the fact that the observed wave profiles depend in a complex, mostly implicit way on the underlying kinematics, making the elaboration of an inversion procedure both a necessary and complex task. In this section, we gather the required kinematics (and the minimal dynamics) needed to fulfill this objective.

This section addresses test particle kinematics (section 2.1), streamlines (section 2.2), surface density and optical depth (section 2.3), and finally discusses the link between radius and semi-major axis (section 2.4), which plays an important role in the inversion procedure. Particular attention is paid to the discussion of the generality of the kinematic model and dynamical constraints used in our inversion procedure.

2.1 Test Particle Kinematics

We consider a satellite orbiting in the equatorial plane of the planet. The cylindrical coordinates are denoted by (r, θ) , where r is the radius and θ is the longitude. We use the subscript s to characterize the satellite.

As in Goldreich and Tremaine (1982), one can linearize the equations of motion of a test particle orbiting the planet to obtain

$$\frac{d^2 r}{dt^2} - r \left(\frac{d\theta}{dt} \right)^2 = -\frac{\partial \Phi}{\partial r} \quad \text{and} \quad (1)$$

$$\frac{d}{dt} \left(r^2 \frac{d\theta}{dt} \right) = -\frac{\partial \Phi}{\partial r}, \quad (2)$$

where

$$\Phi = \Phi_p + \Phi_s \quad (3)$$

is the sum of the planet potential and the satellite potential, to obtain the first order solution for r and θ .

At any given time t , the satellite potential exerted on a particle at (r, θ) is periodic in $(\theta - \theta_s)$. Furthermore, the satellite makes an epicyclic oscillation at angular frequency κ_s , the epicyclic frequency, about a guiding center which revolves at the rate Ω_s , the mean motion. Thus the satellite potential can be expanded in a double Fourier series, one in longitude and one in time:

$$\Phi_s(r, \theta, t) = \sum_{m=0}^{+\infty} \sum_{k=-\infty}^{+\infty} \Phi_{mk} \cos [m(\theta - \theta_s) + k\kappa_s(t - t_0)], \quad (4)$$

where the integers m and k characterize each term of the series and t_0 is the time of satellite periape. The pattern speed

$$\Omega_p = \Omega_s + \frac{k}{m}\kappa_s, \quad (5)$$

is the angular speed of the rotating frame in which the (m, k) component of the satellite potential is stationary.

Denoting by Ω_0 the angular rate of the ring particle in the zero order solution of Eqs. (1) and (2) for r and θ , the first order solution is singular if $\Omega_p = \Omega_0$ (corotation resonance) or if $m(\Omega_0 - \Omega_p) = \pm\kappa$ (Lindblad resonance). Inner Lindblad resonances correspond to the $+$ sign and occur in a ring inside the satellite, and outer Lindblad resonances correspond to the $-$ sign and occur in a ring outside the satellite. We will restrict ourselves here to inner Lindblad resonances. The resonance is labeled $(m + k) : (m - 1)$ because we have

$$\frac{\Omega_0}{\Omega_s} \simeq \frac{m + k}{m - 1}, \quad (6)$$

an approximation that we note here but will not use in the remainder of this paper.

Near a Lindblad resonance, the linear response of a test particle is given by:

$$r = r_0 + \frac{A_r}{\Delta r} \cos m\phi, \quad (7)$$

$$\theta = \theta_0 + \Omega_0 t + \frac{A_\theta}{\Delta r} \sin m\phi, \quad (8)$$

where Δr is the distance from the resonance and

$$m\phi = m [\theta - \theta_{s0} - \Omega_p(t - t_0)], \quad (9)$$

with

$$\theta_{s0} = \theta_s(t_0). \quad (10)$$

The coefficients A_r and A_θ are given explicitly in Goldreich and Tremaine (1982).

As noted earlier, the amplitude of the first order solution for r and θ becomes infinite at the resonance location. The linearization assumption that the first order solution is much smaller than the zeroth order solution breaks down too close to the resonance.

2.2 Streamlines

When considering *fluid* particle motions instead of test particle ones, it turns out that collective interactions (collisions and self-gravity) prevent the divergence just mentioned from occurring; they also make the description in terms of first order deviations from circularity valid to a high level of precision (relative deviations are typically of the order of 10^{-5} or 10^{-4} in observed density waves, an order of magnitude that can be deduced either from linear theory or from order of magnitude analysis of the data; see Longaretti and Borderies 1986 for details), while changing the amplitude and phase of this first order description. Because waves are forced by external satellites and because self-gravity acts as a cohesive force on wave motions, fluid particles sharing the same semi-major axis are expected to follow the same m -lobe orbit, or streamline, in the frame rotating with the pattern speed associated with the considered satellite resonance [see Eq. (5)]. The shape of ring streamlines is given by:

$$r = a [1 - e(a) \cos(m\phi + m\Delta(a))], \quad (11)$$

where a is a semi-major axis, $e(a) \ll 1$ is the eccentricity, and $\Delta(a)$ is a lag angle; as in the previous section, ϕ is the azimuth in the rotating frame. The lag angle has a direct geometric interpretation: it is the angle by which the m -lobe shape of the wave rotates when moving from one streamline to the next [see Fig. 1 where ψ is defined by Eq. (22)].

This description implicitly assumes a Lagrangian approach to fluid motions. An unperturbed fluid particle follows a circular orbit, and has coordinates a, ϕ . Once perturbed, this same particle follows an m -lobe orbit and has coordinates $r(a, \phi), \theta(a, \phi)$, where $r(a, \phi)$ is the relation above and

$$\theta = \phi + 2\frac{\Omega}{\kappa}e \sin(m\phi + m\Delta). \quad (12)$$

In this description, a, ϕ are used as Lagrangian labels of individual fluid particles, instead of the more customary initial position r_0, θ_0 . It is important to note that a, ϕ are both the unperturbed position of the fluid particle, and its Lagrangian labels. Functions of space, such as the ring surface density, are either specified in terms of r, θ or, more often, as a function of a, ϕ through the change of variables defined by the two previous relations.

Eqs. (11) and (12) can either be viewed as an *a priori* assumption concerning fluid particles kinematics, to be validated through the derivation of appropriate dynamical solutions of the equations, an approach adopted in Borderies et al. (1986); or it can be derived from *ab initio* analysis of these same equations, as in Shu et al. (1985c). Note however that Eq. (11), the most important of the two, constitutes in practice the most general such relation one can assume: the fluid particle re-

sponse must be periodic in $m\phi$ because the satellite forcing is¹; and the magnitude of the observed deviations from circularity ensures that a sinusoidal periodic response (the first term expansion of any periodic response) will accurately represent the data to their current level of precision.

For our purposes, Equation (11) involves several implicit features. The first one is that the streamlines do not cross. Non-interacting streamlines would cross at locations where $\partial r/\partial a = 0$; indeed, wherever a difference in semi-major axis δa would not produce a difference in radius $\delta r = \partial r/\partial a \delta a$ at a given azimuth, fluid particles with different semi-major axes would occupy the same location, leading to streamline crossing. One has²:

$$J = \frac{\partial r}{\partial a|_{\phi}} = 1 - q \cos(m\phi + m\Delta + \gamma), \quad (13)$$

where we have neglected the small term $e \cos(m\phi + m\Delta)$ and with:

$$q \cos \gamma = a \frac{de}{da}, \quad (14)$$

$$q \sin \gamma = mae \frac{d\Delta}{da}. \quad (15)$$

In Eq. (13), the lag angle between streamlines is defined by Eq. (11) and γ and q are defined by Eqs. (14) and (15). Equation (13) is a mathematical consequence of Eq. (11) and requires no extra physical input. Streamline crossing is prevented as long as $q < 1$. It is known from observations that although e is a very small parameter, q is usually a significant fraction of unity. The physical meaning of q and γ will be further illustrated in the section devoted to the surface density, 2.3.

From a dynamical point of view, as all forces are small compared to the planet attraction, fluid particles must follow perturbed epicyclic orbits, very much like test particles follow perturbed elliptic (or possibly epicyclic) orbits. This fluid particle epicyclic theory (see Borderies and Longaretti 1987, Longaretti and Borderies 1991, and Borderies-Rappaport and Longaretti 1994) was devised to put the streamline formalism on a more self-consistent footing. For an *ab initio* construction of the streamline formalism, see Longaretti (1992). We have:

$$r = a [1 - e \cos(\theta - \varpi)], \quad (16)$$

with:

$$\varpi = \varpi_0 + \dot{\varpi}(t - t_0), \quad (17)$$

where $\dot{\varpi} = \Omega - \kappa$ is the fluid particle apse precession rate.

Equations (11) and (16) are compatible if (to lowest order in eccentricity):

$$(m - 1)\theta_0 - \varpi_0 - m\theta_{s0} - m\Delta = 0, \quad (18)$$

¹Only the lowest terms in eccentricity are important.

²The name J stems from the fact that $\partial r/\partial a$ is the leading order term in eccentricity in the expression of the Jacobian of the change of variable from r, θ to a, ϕ .

and:

$$m(\Omega - \Omega_p) = \Omega - \dot{\varpi}. \quad (19)$$

Equation (18) expresses the constraint that all fluid particles with the same semi-major axis belong to the same m -lobe streamline. This is a generalization of the condition that an elliptical ring is such that all the particles with the same semi-major axis have the same periapsis angle.

Equation (19) looks like the resonance condition, but it includes all the perturbations exerted on the particles (whose dominant contributions is on the precession rate), in line with the general philosophy of osculating elements; as such it applies throughout the wave region (see Borderies et al. 1986). This description is useful as long as all these perturbations (arising from interparticle collisions and self-gravity, mostly) are much smaller than the effects of the planet, a condition largely satisfied in ring systems. As a consequence, the streamlines do not differ much from the orbits of test particles viewed in the rotating frame. Note that as long as explicit expressions of the forces are not used, the dynamical content of Eq. (19) is absolutely generic, as the osculating epicyclic theory is mathematically equivalent to the generic form of the equations of fluid motion in the limit of small deviations from circularity. As such, this condition is simply a kinematic consequence of Eq. (11). Equation (12) is valid to the same degree of generality.

The angle Δ [defined by Eq. (11)] is introduced because the streamline orientation varies smoothly from the inside to the outside of the resonance. Indeed, in Eq. (19), the secular drift of $m(\Omega - \Omega_p) - \kappa$ that would be due to the planet alone can be compensated by self-gravity (a condition that by itself yields back the wave dispersion relation; see, e.g., Borderies et al. 1986 and Longaretti 1992). But since self-gravity is a small force, this compensation takes place only if the shift of Δ between streamlines is large enough, *i.e.* if we are in the condition of the tight-winding approximation:

$$ma \frac{d\Delta}{da} \gg 1, \quad (20)$$

This is why density waves are so tightly-wound in rings. In spiral galaxies, the self-gravity dominates the force due to the central bulge, radial excursions are much larger (so that a first order deviation from circular motions such as the one adopted here is much less appropriate) and the spiral arms are much more open. The equations describing linear waves can be recovered the limit where $q \ll 1$ (Longaretti and Borderies 1986).

Another useful qualitative dynamical feature relates to the WKBJ ordering, which is usually assumed in theoretical analyses of density waves. Let us point out the meaning of this approximation for our purposes. A wave possesses three radial scales³: the semi-major axis, the wavelength l (note that the radial wavenumber $k \simeq m(d\Delta/da)$, a near-equality that holds to leading WKBJ order), and the scale of variation of the wave amplitude and background⁴, which we will denote ξ . In order of magnitude, for a typical wave, $a \sim 10^5$ km, $l \sim 10$ km, and $\xi \gtrsim 10l$ (as waves

³A fourth radial scale is obtained from ae . This scale is smaller than any of the other three, and is not required in this discussion.

⁴For instance, the lengths over which the amplitude of the wave increases and decreases – the damping scale, or the length of the wavetrain.

propagate for a few to a few tens of wavelengths). The WKBJ ordering holds when the variation of the wave phase function ($m\Delta + \gamma$) with radius is much faster than the variation of the wave amplitude, *i.e.*, $k\xi \gg 1$. Eqs. (14) and (15) imply then that $q \cos \gamma \sim ae/\xi \ll q \sin \gamma \simeq kae$ and that $\gamma \simeq \pi/2$ when the WKBJ ordering holds. Also, as all density waves excited at inner Lindblad resonances display decreasing wavelength and decreasing amplitude q with increasing radius (at least in the far propagation region for the amplitude), and as $q \simeq kae$, the decreasing amplitude is related to a decrease of the eccentricity on scale ξ .

The WKBJ ordering ($k\xi \gg 1$) is satisfied in Saturn’s rings, albeit to a much lesser degree of precision than the tight-winding approximation ($ka \gg 1$). This motivates us to assume that most of the radial variation of the wave is due to the dependence of the lag angle Δ on semi-major axis. We nevertheless devise a correction to account for the imperfection of the WKBJ ordering, as a precise determination of the phase function is essential to the robustness of our procedure.

Note that both the linear (e.g., Shu 1984 and references therein) and nonlinear (e.g., Shu et al. 1985c and Borderies et al. 1986) density wave dispersion relations imply that $k \rightarrow 0$ at the resonance radius, so that the WKBJ ordering *must* fail there and $\gamma \simeq 0$ in the evanescent part of the wave and close to the resonance. This fact limits our ability to reconstruct the wave kinematics inside the first wavelength, a point that will be further discussed later on.

For future reference, we stress that several different “phases” are used in this paper, and introduce some terminology to distinguish them. These phases are the lag angle Δ , the phase function defined by:

$$f(a) = m\Delta(a) + \gamma(a), \quad (21)$$

and the profile phase ψ :

$$\psi = m\phi + f. \quad (22)$$

The phase function is a characteristic of the wave (*i.e.* all the profiles have the same phase function) and the profile phase characterizes the location of peaks and troughs in 2D as well as in each 1D wave profile. The profile phase is the one which may be associated to the usual concept of wave phase; e.g., the density maxima in the (a, ϕ) plane correspond to $\psi = 2\pi$ modulo 2π in the WKBJ ordering, while minima correspond to $\psi = \pi$ modulo 2π (see Fig. 1). The phase function is a useful intermediate quantity which gathers the semi-major axis dependence of the profile phase, and whose derivative is, by definition, the radial wavenumber.

Summary: This subsection (as well as the previous one) has introduced and discussed a number of elements of wave kinematics and dynamics. In our reconstruction procedure, the only kinematic relation introduced here that we use is Eq. (11) and its mathematical consequence Eq. (13), along with Eq. (12). We have argued that they are quite general; furthermore, Eq. (12) is used only in a limited way, to justify that the difference between θ and ϕ can be ignored, a consequence of $e \ll q$. The only piece of dynamics used is the WKBJ ordering, *i.e.*, the fact that the radial variation of the lag angle $m\Delta$ is much larger than the variation of amplitudes and background e , q , and Σ_0 (the ring unperturbed surface density). As a consequence $\gamma \simeq \pi/2$ over most of the wave. As discussed,

this assumption is expected to fail inside the first wavelength, and our simulated data incorporate this feature.

2.3 Surface Mass Density and Optical Depth

As the length scales of the observed wave pattern are much larger than the local ring thickness, it is legitimate to adopt a two-dimensional description. Conservation of the mass of a ring element in the Lagrangian change of variable r, θ to a, ϕ implies that $dM \equiv \Sigma(r, \theta)drd\theta = \Sigma_0(a)|J|dad\phi = \Sigma_0(a)dad\phi$ so that the perturbed surface mass density given by:

$$\Sigma = \frac{\Sigma_0}{1 - q \cos(m\phi + m\Delta + \gamma)}, \quad (23)$$

where we have directly identified the Jacobian of the change of variable with its dominant term in eccentricity given by Eq. (13), while noting that $J > 0$ for $q < 1$; Σ_0 is the unperturbed surface density, also called the background surface density. This follows because the ring mass δM enclosed between these two streamlines is the same between perturbed and unperturbed states ($\delta M = \Sigma\delta r\delta\theta = \Sigma_0\delta a\delta\phi$), and because, to leading order in eccentricity, the Jacobian of the change of variable from a, ϕ to r, θ reduces to J .

This relation provides us with another meaning for q : at peaks, $\sigma = \Sigma_o/(1-q)$ while at troughs, $\sigma = \Sigma_o/(1+q)$. Therefore q measures both the density variation due to the wave propagation, and its nonlinearity, and γ measures the relative contribution of the variations in eccentricity and lag angle to this density contrast [see Eqs. (14) and (15)]. Only the lag angle contribution to the density contrast has been used in Fig. 1 (consistent with the WKBJ ordering); this figure also illustrates that the variation of distance of the streamlines is the direct cause of the surface density variations of the wave, consistently with Eqs. (23) and (13).

Application of Eq. (23) to the ring normal optical depth τ is usually taken for granted, but requires some discussion. For simplicity, assume that the ring particle distribution with respect to size, spin, shape, etc. can be represented by a discrete index i , and let $N_i(r, \theta)$ be the column density of particles of type i , m_i their mass, and S_i their cross-section. With these definitions, the ring surface density $\Sigma(r, \theta) = \sum N_i m_i$ while its optical depth $\tau(r, \theta) = \sum N_i S_i$. If the distribution is constant in time, the formal similarity between these two relations implies that the optical depth τ will also formally obey Eq. (23), as mass conservation then reduces to number conservation and as the wave restoring force (the self-gravity) does not induce particle segregation. In such a context, the optical depth is therefore also given by

$$\tau = \frac{\tau_0}{1 - q \cos(m\phi + m\Delta + \gamma)}, \quad (24)$$

where $\tau_0(a)$ is the "unperturbed" optical depth⁵.

The remarks above show also that the same relation will hold to a high degree of precision if the size distribution, in particular, is evolving slowly in comparison to the dynamical time-scale

⁵i.e., the optical depth that would be found if the deviations from circular motions were suppressed, but this may differ from the optical depth outside the wave propagation region; see the following discussion.

of the wave. This depends in turn on the efficiency of gravitational accretion in the ring region. Weidenschilling et al. (1984) put forward and studied the concept of *Dynamical Ephemeral Bodies*, or DEBs. This concept leads to a particle size distribution evolving on the time-scale of a rotation period Ω^{-1} (Longaretti, 1989), but requires that the efficiency of gravitational accretion is large and only mildly variable throughout a sizeable fraction of the ring to account for the remarkably ubiquitous size distribution found by Zebker et al. (1985). However, a recent reinvestigation of the efficiency of gravitational accretion by means of numerical simulations shows that this is most likely not the case, largely independently of particle collisional properties (Karjalainen and Salo, 2004). Because the dispersion velocity of ring particles is so small, even in perturbed regions, this implies in turn that, on average, only minute fragments of particles can be collisionally eroded from or accreted onto ring particles, leading to very long time-scales for the evolution of the particle size distribution, validating the use of Eq. (24), at least with respect to this issue. Note that the particle-size distribution within the wave may be different from the particle size distribution outside the wave, because the collisional regime is different. In this respect, the spectral “halos” found by Nicholson et al. (2008) may indicate a variation in particle sizes in the vicinity of strong density waves compared to other ring regions. In any case, the presence of the wave certainly changes the particle velocity dispersion and therefore the collisional regime, leading to evolution of the particle size distribution on long enough time scales throughout the wave region. This may be accounted for by allowing the opacity $K = \tau/\Sigma$ to depend on semi-major axis (any possible dependence on the azimuthal direction being quickly erased by the ring velocity shear).

A related issue concerns the presence of self-gravity wakes, as such structures form and dissolve on time scales comparable to the orbital period (see also Karjalainen and Salo 2004 and references therein). It is unclear at this point how the presence of density waves (which locally enhance or reduce the density) affect the existence and properties of wakes, and how such wakes might affect the optical depth profiles in the wave region. Also, wakes, and more generally regions where the particles are closely-packed (as may be the case in sections of the B ring or in density wave maxima), certainly affect the way the optical depth is reconstructed from the raw data.

These last issues are difficult to quantify. We therefore ignore them for the time being, but we keep in mind that they may affect in an uncontrolled way the application to real data of the reconstruction method developed here.

In the simulated data presented here, we have assumed for simplicity that the opacity $K = \tau/\Sigma = \tau_0/\Sigma_0$ is constant, so that specifying τ_0 as a function of semi-major axis also specifies the radial dependence of the surface density. We also ran simulations with a variable opacity, with no impact on the precision of the reconstruction method.

2.4 Kinematics, and the link between radius and Semi-Major Axis

We have introduced a number of functions of semi-major axis: $e(a)$, $\Delta(a)$, $q(a)$, $\gamma(a)$, $\Sigma_0(a)$, $\tau_0(a)$. These are the fundamental kinematic functions that our procedure aims at extracting from the data; they completely specify the wave kinematics. Note that the recovery of Σ_0 from actual data requires some dynamical input, e.g., the nonlinear dispersion relation; at the level of precision we aim at in the end, uncertainties in the modeling of the ring stress tensor may affect the

reconstruction of Σ_0 , a question we will only briefly touch upon here.

Furthermore, we have used a and ϕ as a set of spatial coordinates; *e.g.*, the surface density of the previous section is spatially prescribed in terms of a and ϕ . However, the data are given as a function of the radius r and azimuth θ . Thus there is a need to apply transformations from a, ϕ to r, θ and vice-versa.

One can check that assuming $\theta = \phi$ in such a change of variable leads to negligible error at the level of precision achieved in the data, due to the magnitude of the eccentricity, and the way it comes into play in the change of variables (see Appendix A.1). Furthermore, in the radio occultation profiles, the data acquisition procedure ensures that one can assume that θ (and consequently ϕ) is constant in a given profile⁶, with negligible error at the level of precision of the data (see next section). Therefore, it is legitimate to assume $\Sigma(r, \theta) = \Sigma(r, \phi)$ (or a similar relation for τ), but one needs to specify how $\Sigma(a, \phi)$ is deduced from $\Sigma(r, \phi)$.

Eq. (11) allows one to compute the radius r as a function of the semi-major axis a and azimuth ϕ as long as the functions $e(a)$ and $\Delta(a)$ are known; from our previous remarks, $m\phi$ can be considered as a constant parameter depending only on the optical depth profile considered, so that this relation can be viewed as an $r(a)$ relation, and can be inverted to find $a(r)$. The details of this inversion procedure are discussed in Appendix A.1.

Note that even though ae is a small quantity compared to the wavelength, it induces a difference between $\tau(a)$ and $\tau(r)$, which can produce a significant error in the determination of q and τ_0 , and cannot be neglected.

3 Simulated Data

In order for our simulated data to be realistic, we have extracted some of the required parameters (such as longitudes and times) from the diffraction-reconstructed occultation data for the eight Cassini Radio Science Team occultation experiments (Kliore et al., 2004) that will be used later on as a real test case of our method. These data were acquired on days 123 (May 3rd), 141 (May 21st), 177 (June 26th), and 214 (August 2nd), respectively, of 2005. On each day there was both an ingress and an egress experiment, for a total of eight profiles. For each profile, the data were acquired at the Deep Space Stations (DSS) of the Deep Space Network DSS-14, DSS-43, DSS-43, DSS-63, DSS-14, DSS-14, DSS-63, and DSS-63, respectively. The X-band data (frequency of 8.4 GHz) are plotted in blue in Fig. 8 with a resolution of 1 km, with one point every 250 meters⁷, for the Mimas 5:3 density wave. This wave, propagating from an inner Lindblad resonance location of 132301 km from Saturn's center, is one of the strongest and most nonlinear waves in the rings. It was particularly studied by Longaretti and Borderies (1986). These data have a free space signal-to-noise ratio⁸ of 54 dB-Hz. The instrumental noise is generally very low, although it is larger at the peaks. Peaks that reach an optical depth of 5 are not physical because they exceed the RSS

⁶This is not in general true for stellar occultations.

⁷The sampling rate of the diffraction-limited data is 250 m, and when diffraction is removed the effective spatial resolution is 1 km (Marouf et al. 1986).

⁸Defined as $10 \log_{10}(\text{averaged carrier power} / \text{average noise power in 1 Hz bandwidth})$.

capabilities; in other words, we have no data points for the tops of these peaks. In addition to the instrumental noise, the data also contain unmodeled physical effects, such as peak shoulders and split peaks.

We consider each occultation of a given feature to be instantaneous with its time t being the mean time of the occultation. This assumption introduces negligible error, as can be checked by comparing the total data acquisition time for this wave (~ 15 seconds for the Mimas 5:3 density wave) with the dynamical time-scale associated with the pattern speed (18.1 hours for the Mimas 5:3 density wave). We also assume that the ring intercept point of the spacecraft-to-Earth ray occurs at a constant mean inertial longitude θ . This assumption is justified for nearly diametric occultations, such as the ones considered, which typically cover a longitude variation of 0.01° . Therefore, we have one value of $m\phi$ for each occultation. These values are shown in Table 1.

We used these values of $m\phi$ and constructed eight simulated occultation profiles in the following way. First we defined the parameters $ae(a)$ and $\tau_0(a)$ using the array of radii of the actual profiles as semi-major axes and the empirical equations:

$$ae(a) = 0.1 + 2 \left[1 + \tanh \left(\frac{a - a_c}{\zeta} \right) \right] \left[\frac{a - a_N}{a_1 - a_N} \right], \quad (25)$$

$$\tau_0(a) = 0.5 + 0.5 \left[1 + \tanh \left(\frac{a - a_c}{\zeta} \right) \right] \left[\frac{a - a_N}{a_1 - a_N} \right], \quad (26)$$

where a_1 (about⁹ 132260 km) is the first (smallest) semi-major axis, and a_N (about 132470) is the last (largest) semi-major axis; $a_c = 132275$ km and $\zeta = 50$ km. We selected $a_1 = a_{res}$ as the resonance location for the simulated data. These choices are made so that the resulting profiles loosely resemble the observed wave. The choice of $\tau_0(a)$, which increases at the beginning of the wave, is consistent with the calculations of Shu et al. (1985b) and Borderies et al. (1986), who find that the surface density is enhanced in the wave zone outward of the resonance. This is a general feature of strong waves.

Next, we defined the opacity K , and having the background optical depth, this allowed us to compute the background surface density Σ_0 in each point. As mentioned above, the simulated data used in this paper have a constant opacity, which is $K = 0.0125$ cm²/g. We also made tests with an opacity varying with the semi-major axis.

The parameters $m\Delta$ and q are next constrained in each point by enforcing the ideal (WKBJ, pressureless, dissipation free) nonlinear dispersion relation throughout the wave region. This is certainly not satisfied in actual waves, but provides a convenient way to test our ability to reconstruct all kinematic parameters, including the surface density, in the wave propagation region. The parameters $m\Delta$ and q are computed iteratively in the following way. Before starting the iterative calculation, we computed in each point $q \cos \gamma$ from Eqs. (14) and (25), and we initialized $m\Delta(a_1) = 0$. Next we computed:

⁹This value is in fact the initial radius of our simulated data instead of its semi-major axis. A similar comment applies to a_N .

$$m\Delta(a_n) = m\Delta(a_{n-1}) + \int_{a_{n-1}}^{a_n} k da, \quad (27)$$

where the wavenumber k comes from the dispersion relation (Borderies et al., 1986):

$$k = \frac{3(m-1)\Omega^2}{2\pi G\Sigma_0 C(q)} \frac{(a - a_{res})}{a_{res}}; \quad (28)$$

in this equation, Ω is the mean motion at a_{res} , G is the gravitational constant, and:

$$C(q) = \frac{4}{\pi} \int_0^{+\infty} du \frac{\sin^2 u}{u^2} H\left(\frac{q^2 \sin^2 u}{u^2}\right), \quad (29)$$

with:

$$H(q^2) = \frac{1 - \sqrt{1 - q^2}}{q^2 \sqrt{1 - q^2}}. \quad (30)$$

Having $m\Delta$, it is possible to compute $q \sin \gamma$ from Eq. (15) and then q . We iterate the calculations until the maximum change in the values of q at the same point and between iterations is less than 0.01. At the first iteration, $C(q) = 1$ (i.e., the dispersion relation reduces to the linear one).

The parameter γ is computed from Eqs. (14) and (15); f is then derived from Eq. (21). The simulated wave parameters are shown in Fig. 2. Note that γ increases from 0 to $\pi/2$ for the first thirty km of the wave, so that in this region, our simulated data are not consistent with the dynamics of a real wave (as the dispersion relation fails there), although self-consistency of the kinematics has been enforced in the way the simulated data have been constructed. The simulated data nevertheless resemble an actual wave in the first wavelength. The failure of the WKBJ ordering inside the first wavelength is consistent with the findings of Longaretti and Borderies (1986) for the Mimas 5:3 density wave. In this portion of the wave and farther, q increases as the wave becomes more and more nonlinear until its growth (implied by self-gravitational stresses) is stabilized to a plateau and then damped by viscous stresses. Our simulated data also loosely reproduce this behavior.

Profiles without noise were derived from the above simulated kinematic parameters, the values of $m\phi$, and Eqs. (11), (22), and (24). These profiles are shown by the blue lines in Fig. 4. The red lines on top of the blue lines represent the reconstructed profiles, which will be discussed in section 4.3.

Next, we applied eight shifts in radii representing our imperfect knowledge of the absolute radial scale in actual wave profile recording. These shifts are 0, -0.5, -1.0, 0.5, 1.0, -1.0, -1.5, 1.5 km. In other words, the first synthetic profile without noise was not shifted, the second one was shifted by -0.5 km, the third one by -1.0 km, etc. The ability to recover the values of these radial shifts will be one test of our analysis method.

Next, we generated noisy data from the shifted profiles without noise. For this, we used the actual data from 131980 km to 132190 km, i.e. inward the Mimas 5:3 density wave profiles, in a region where the optical depth fluctuations are somewhat muted. We could have used free space data, but these data contain very little noise. Our assumption was that whatever physical effects

give rise to optical depth fluctuations in the region inward of the density wave plausibly acts also in the density wave. We used the actual optical depths of each profile in the region considered and inferred the amplitudes of the signal. For each profile, we detrended the amplitudes by removing a parabola. We computed the standard deviation of the detrended amplitudes. We generated an array of pseudo-random values drawn from a normal distribution with a mean of zero and standard deviation that is twice the standard deviation of the detrended amplitudes. We averaged over four consecutive samples to produce an array of amplitude noise. This technique was used because the resolution of the data is 1 km, but they are sampled at 250 m intervals. We added this noise to the amplitude of the simulated data without noise, and hence generated noisy simulated data. The noise in these data is not instrumental noise, it represents a real effect resulting from real fluctuations in the optical depth (Showalter and Nicholson 1990). The noisy profiles are shown by the blue lines in Fig. 5. Again, the red lines on top of the blue lines represent the reconstructed profiles, which will be discussed in section 4.3.

The simulated profiles were interpolated to a common radial scale extending from 132260 km (the assumed resonance radius) to 132470 km, with a step-size of 250 m as in the actual data. As mentioned above, our goal was to generate plausible-looking profiles for which the wave parameters are known, rather than accurately replicating the Mimas 5:3 profiles. These simulated profiles were used to establish the procedure which is described in the next section. We chose the example of the Mimas 5:3 density wave to guide us for generating the simulated profiles because this wave is clearly visible and isolated in the data, and has previously been studied by Longaretti and Borderies (1986). The analysis of Longaretti and Borderies (1986) used only one optical depth profile (a photopolarimeter profile), which did not allow us to accurately constrain the location of the peaks, the background optical depth, and the nonlinearity parameter q . In this paper, we will apply the procedure to eight actual Mimas 5:3 radio optical depth profiles.

4 Procedure

4.1 Outline of the inversion procedure

Observations (or simulated data) provide us with $\tau(r, \theta) = \tau(r, \phi)$ at specific azimuths ϕ (in the frame rotating with the pattern speed). These observations are modeled using $\tau(a, \phi)$ given by Eq. (24), using the $a(r)$ relation discussed in section 2.4 and Appendix A.1, so that $\tau(r, \phi) = \tau(a(r), \phi)$. They involve three “secondary” functions of semi-major axis: the unperturbed optical depth τ_0 , the nonlinearity parameter q and the phase function f (Eq. 21). Furthermore, the quantities q and f depend on the “primary” kinematic quantities, *i.e.* the eccentricity e and the lag angle Δ (one can choose γ instead), through Eqs. (14), (15), and (21). Our objective is to recover the five functions $\tau_0(a)$, $q(a)$, $m\Delta(a)$, $ae(a)$, and $\gamma(a)$ from the data. The major *a priori* difficulty lies in the fact that the relation between $\tau(r)$ and $\tau(a)$ at any given azimuth involves the knowledge of e and γ , which are not known beforehand when fitting Eq. (24) to the data. This makes the recovery of a common set of kinematic parameters for all profiles a challenging task.

One possible method of inversion that would circumvent this problem would be to perform a least-squares fit for each radius (and at all radii at the same time), to the five previous parameters

with the help of the $\tau(a, \phi)$ and $a(r)$ relations. As one has more profiles than unknowns, this procedure would seem to be well-posed, and would have a definite advantage: no dynamical assumption of any kind (such as the WKBJ ordering) would be required, only generically valid kinematic constraints would be used. We have tried this, and, unfortunately, this fails for several reasons. First, the number of profiles is limited, and some of them have similar values of $m\phi$, so that they barely provide enough independent information. For a simulation, we could have used more profiles and a good sampling of values of $m\phi$, but we wanted to see what we could do with the Radio Science data that have been pre-processed so far. Secondly, the inversion procedure is always extremely sensitive to errors in the determination of the phase function f , so that, unless provided with a guess unrealistically close to the actual phase function, an iterative global least-squares procedure was found to fail systematically. Thirdly, the radial origin of reference of all the profiles is not the same, so that one must also fit for the radial shifts one needs to apply to normalize the radial scales. In the future we will know the radial absolute scale to within 100 meters, but again we wanted to see what we could do with the existing Radio Science profiles. Note that even without radial scale uncertainty, the resonance locations vary with time due to the long period variation of the orbits of satellites such as e.g. Mimas and Pandora. We found that radial shifts considerably worsen the question of the precise determination of the phase function in a global least squares fit. Fourthly, the smallness of the wave amplitude and the loss of the WKBJ ordering in the vicinity of the wave resonance makes the least-squares procedure less sensitive to variations of $m\Delta$ in this region of the wave. Finally, the relations between q and f on the one hand, and e and γ on the other, involve a radial derivative; it is difficult to have these derivatives numerically well-behaved in a global fitting procedure. These difficulties make the identification of a common set of kinematic parameters for all profiles nearly impossible. Nevertheless, a least-squares global fit may be used as a final step to improve the quality of the fit, a point we have not yet checked in any detail due to practical implementation difficulties.

Instead, we have reverted to the approach devised by Longaretti and Borderies (1986), with a number of significant improvements. The inversion procedure is constructed from the iteration of two main stages. In the first one, the secondary quantities $\tau_0(a)$, $q(a)$ and $f(a)$ are deduced from the data for given primary parameters $e(a)$ and $\gamma(a)$ (which provide us with a given $a(r)$ relationship); this step relies on the WKBJ ordering, which we have shown to be valid at least in the nonlinear part of density waves, but we incorporate corrections due to the imperfection of this ordering. In a second stage, $e(a)$ and $\gamma(a)$ are redetermined from the $q(a)$ and $f(a)$ just obtained, with the use of Eqs. (14), (15), and (21); the WKBJ ordering is also used for convenience in this stage, but this is not strictly necessary. Determination of the radial shifts of the profile with respect to a common radial scale are interweaved in these steps in a manner that will be specified below. These two stages are iterated to improve the determination of $\tau_0(a)$, $q(a)$ and $f(a)$ on the one hand, and $e(a)$ and $\gamma(a)$ on the other. Iterations proceed until convergence is achieved. We now turn to a more explicit and detailed description of these two stages.

First, an initialization of all quantities is required before any iteration is applied. This initialization and its rationale are described in the next subsection.

Next, we present the first stage (recovery of the secondary parameters), which is broken up into several steps. The first one (subsection 4.3) describes the determination of the secondary

parameters τ_0 , q , and ψ as a function of the semi-major axis in the vicinity of the peaks for each of the various profiles. This is the most complex step of our inversion procedure; it relies on the WKBJ ordering. However, since a precise determination of the phase function turns out to be critical in our inversion procedure, we apply in this step a correction to the leading order WKBJ solution for ψ by taking into account the small but non-vanishing variation of the wave amplitude compared to the variation of the profile phase; this correction might not always or everywhere be useful, but is systematically computed, for simplicity. In the second step (subsection 4.4), we determine the global phase function f from the profile phase ψ as well as a first approximation of the radial shift for each profile. We also make use of these profile radial shifts to “unshift” the data as well as τ_0 , q , and f such that they are on a common radial scale. The last step determines the mean secondary parameters τ_0 , q and f common to all profiles (subsection 4.5).

The second stage is divided into two steps: recovery of the primary kinematic parameters e and γ (and coincidentally, $m\Delta$) from the mean secondary parameters q and f (subsection 4.6), and final fitting of the reconstructed profiles $\tau(r, \phi)$ on the data, which allows us to determine an additional correction to the radial shift of the profiles (subsection 4.7). This correction is needed because first we are dealing with an iterative process with several passes through the first and second stages, and second, we are making assumptions that are only approximations, *e.g.*, that τ_0 and q are constant locally around each peak. The wave kinematic parameters τ_0 , q , f , ae , and γ are shifted by the same amount as the profiles.

The WKBJ ordering is primarily needed in the first step of the first stage, and, to the same degree of approximation, in the recovery of e and γ . The $a(r)$ relation is needed in the first step of the first stage and in the last step of the second stage. Also, as will be shown shortly, this ordering implies that using only information at the profile peaks¹⁰ or in the vicinity of the peaks minimizes errors in the knowledge of e and (small) deviations of γ from $\pi/2$. Because all five kinematic parameters we wish to recover vary smoothly enough with semi-major axis, their determination at the peaks of the profiles is sufficient to constrain them throughout the wave region. Information is therefore gathered in the vicinity of peaks only in the first steps of our procedure. This limited information is sufficient to precisely reconstruct the wave kinematics, but naturally, the goodness of the fit is checked throughout the wave region by the reconstruction of the profiles.

In practice, the WKBJ ordering, as already mentioned, is not robust enough in the first wavelength region (and in the evanescent region as well); this is true of actual data, as found by Longaretti and Borderies (1986), and of our simulated data as well. As will be seen, even in this region, our reconstruction method does not entirely fail, but does not provide good enough results for our ulterior purpose of torque measurement. Because of this limitation, practical physical diagnostics of wave and disk physics may require us to apply extraneous constraints to this inner wave region. This point will be further discussed in our conclusion section.

Our inversion procedure makes use of three different iterative processes: one for the computation of $a(r)$ (see appendix A.1), one for the recovery of e and γ (see appendix A.2), and the entire procedure itself. We found that, in general, three iterations of the whole inversion process were

¹⁰The same argument holds at troughs. However, peak locations are much more precisely defined than troughs, although the experimental noise is larger there; only peaks will be used in the procedure outlined in this paper. The neglect of the troughs is compensated by the fact that we have many profiles, whose peaks occur at different radii.

sufficient to achieve convergence to a high level of precision, with and without noise superimposed on our synthetic profiles. Iterations of the whole inversion procedure are referred to as “passes” in the remainder of the paper.

The reader may ask why such an involved inversion procedure is required. We found by trial and error that simpler choices either failed entirely, or produced unreliable results. This inversion procedure has been implemented in MATLAB.

4.2 Initialization

Our initialization is designed such that the kinematic parameters can be treated as the results of a fictitious previous pass, for implementation convenience. It assumes that the eccentricity is equal to zero everywhere and that the profiles are not shifted. Thus the semi-major axes are equal to the radii. As explained below, we focus first on the peak regions, where $r = a$ holds to a high level of precision, so initializing $e = 0$ is a reasonable choice to initiate the procedure. For the other parameters, we initially assume $\gamma = \pi/2$ (strict validity of the WKBJ ordering), $f = 0$ (an arbitrary choice, but a better one would be required only if $e \neq 0$, as it is only used in the $a(r)$ relation), $\tau_0 = 1$ (from the behavior of τ at the beginning of the wave), and $q = 0.5$ (midway between its possible minimum and maximum values). For each profile, and for each peak, the peak location is approximated initially by the semi-major axis (or radius) of highest optical depth in a window of data containing the peak.

4.3 Recovery of the secondary parameters: profile phases and peak characteristics

We now come to the crucial problem of determining precisely the peak locations as well as the corresponding τ_0 , q , and ψ of each profile using as initial estimates the results of the previous pass (or of the initialization in the first pass). This is one of the points on which we significantly improve on Longaretti and Borderies (1986). At each pass through our procedure, we first improve the determination of $\psi(a)$ (subsection 4.3.1), and then the determination of the peaks’ characteristics (subsection 4.3.2).

In this step, we treat the various profiles independently.

4.3.1 Profile phase determination:

Consistently with the WKBJ ordering, we note from Figs. 3, 4, and 5 that the large-scale variations of the wave parameters occur over a scale larger than the wavelength. The variations in optical depths (see Eq. 24) are therefore dominated by the variation of ψ (see Eq. 22) with semi-major axis.

Let us first look at what happens if this approximation is exact, *i.e.*, if $\gamma = \pi/2$ exactly throughout the wave region and the variations of q and τ_0 with semi-major axis are negligible; these approximations cannot hold exactly at the same time (we will come to this below), but constitute a useful starting point. In this case, Eq. (24) implies $\psi = 2n\pi$ at peaks (n is an integer, and successive

peaks correspond to successive values of n). It follows that $\cos(m\phi + m\Delta) = \cos(\psi - \gamma) = 0$ and thus $r = a$ at the peaks, so that $\psi(a) = \psi(r)$ at the peaks. We treat the resonance radius as a first “peak” with $f = 0$ (approximately true at resonance) so that $\psi = m\phi$ there (modulo 2π).

It is interesting to note that in the WKBJ approximation, the value of the profile phases at the peaks is independent of the peak locations; this is not quite the case if we take into account the inaccuracy of the WKBJ approximation. To account for this inaccuracy outside the first wavelength¹¹, we compute a correction with the help of the peaks’ characteristics determined in the previous pass (or of the initialization in the first pass, and the correction vanished then) in the following way.

Note that because q and τ_0 are not exactly constant, the assumption that $\tau(r) \equiv \tau(a(r))$ reaches a maximum at points such that $r = a$ is incorrect for several reasons. First, even ignoring the non-constancy of τ_0 and q , τ would indeed be maximum for $\psi = 2n\pi$, but this would not correspond to locations where $r = a$ because $\gamma = \pi/2$ would not be exactly true. Secondly, there may be a model error in that we have taken τ to the lowest order in eccentricity in Eq. (24). Thirdly, τ_0 and q vary. Even though they vary slowly, these variations imply that the maxima of optical depth do not correspond to $\psi = 2n\pi$. Of all three effects, only the third is possibly non-negligible at the level of precision of the data, as can be checked from order of magnitude estimates. The second is negligible due to the very small eccentricities ($< 10^{-4}$, typically). The first is automatically taken into account in our procedure in all passes but the first, although it is negligible except close to the resonance. The third effect is accounted for by computing a first order correction $\delta\psi$ to the phase function, $\psi = 2n\pi + \delta\psi$, at the maxima of $\tau(r)$, due to the non-vanishing derivatives $\tau'_0 \equiv d\tau_0/da$ and $q' \equiv dq/da$. To linear order in $\delta\psi$, the constraint $d\tau/dr = 0$ at the peaks semi-major axis a_{pk} yields:

$$\delta\psi(a_{pk}) = \frac{\tau'_0(a_{pk}) [1 - q(a_{pk})] + \tau_0(a_{pk})q'(a_{pk})}{q(a_{pk})\psi'(a_{pk})\tau_0(a_{pk})}. \quad (31)$$

This correction is appropriate except close to the resonance where $\gamma \sim 0$.

4.3.2 Improved determinations of the peak locations, and of q and τ_0 at the peaks:

The procedure outlined in the previous subsection defines $\psi(a_{pk})$ at the peaks of each profile, and $\psi(a)$ is obtained from $\psi(a_{pk})$ by interpolation; this procedure is quite accurate as $\psi(a)$ varies smoothly enough. Next, we make use of this information to improve the determination of the positions of the peaks, and to determine the values of q and τ_0 at the peaks. To achieve this, we rely again on the fact that these two quantities should be approximately constant in the vicinity of any peak (or of any point for that matter) and find them by least-squares fitting of the optical depth profile in the vicinity of each peak with a function inspired from Eq. (24).

We first define an approximate optical depth profile function that is valid around any peak a_{pk} by

$$\tau_{fit}(a) = \frac{\tau_{0_{pk}}}{[1 - q_{pk} \cos \psi(a)]}, \quad (32)$$

¹¹Inside the first wavelength, as the WKBJ ordering fails anyway, an altogether different reconstruction procedure is required. See the discussion section.

where $\tau_{0_{pk}}$ and q_{pk} are the values of τ_0 and q at the considered peak, and $\psi(a)$ is the profile phase function just determined. The use of an accurate approximation to the true $\psi(a)$ turns out to be crucial for the convergence of our inversion method. We then use this approximate representation of the exact peak profile while allowing for a possible error δ_{pk} in the peak location by defining:

$$\hat{\tau}_{fit}(r) = \tau_{fit}(a(r + \delta_{pk})), \quad (33)$$

which amounts to a radial translation of $\tau(r)$. This expression involves the knowledge of the function $a(r)$, which is obtained from the inversion of $r(a)$ through the process described in Appendix A.1 (in the first pass, $e = 0$ so that $r = a$). This inversion uses the determination of e and $m\Delta$ obtained in the previous pass.

This function is then fitted by least-squares to the actual peak profile in a window around the considered peak. This fit yields the three unknown parameters of the function: q_{pk} , $\tau_{0_{pk}}$ and δ_{pk} . By trial and error, we found that the window was optimal when allowing ψ to vary by $\pm 2\pi/3$ around its peak value; this results from a compromise between the validity of the assumption of constant q and τ_0 around the peak, and the precision of the method.

When $e \neq 0$, $\tau_{fit}(r)$ is narrower in the peak regions than $\tau_{fit}(a)$ which is a characteristic of the actual peak profiles. Due to this property, our procedure results in substantially improved values of q_{pk} and $\tau_{0_{pk}}$ in the second and subsequent passes with respect to the first. Note that δ_{pk} is a peak radial position correction pertaining to each peak, and is not related to the radial shifts applied in section 3 to mimic present inconsistencies in the ring radial scale between actual profile data.

Finally, we update the peaks' semi-major axes to account for the δ_{pk} corrections with the help of the $a(r)$ function, so that, for each peak, we now have better approximations of a_{pk} , $\psi(a_{pk})$, $q(a_{pk}) = q_{pk}$, $\tau_0(a_{pk}) = \tau_{0_{pk}}$. The full functions $\psi(a)$, $q(a)$ and $\tau_0(a)$ are specified by interpolation.

4.4 Recovery of the phase function and first radial scale correction

At this point in our procedure, we have determined the profile phase $\psi(a)$ for each profile. What we need is a single phase function $f(a)$, as precisely determined as possible due to the sensitivity of the procedure to errors in this quantity.

First we compute the phase function for each profile by subtracting $m\phi$ from ψ [see Eq. (22)]. Next we shift the phases by an integer number of 2π . Indeed, the way we have ascribed values to ψ at each peak does not ensure coherence between profiles since peaks in different profiles belonging to the same wavecrest may not correspond to the same value of ψ , which may differ by an integer number of 2π . Once this is done, the various f functions still present some scatter, which is due both to errors in our reconstruction procedure and to differences in the absolute radial scales of the various profiles. We determine a first approximation of these absolute radial scale differences by translating each profile by an integer multiple of 2π to minimize the difference between the phases of the current translated profile and the first profile. In this way we compute a single fixed radial shift for each profile. We call this action ‘‘collapsing the phases’’ because if there were no approximation or assumption in our whole procedure, all the phase functions would coincide after this collapse. This determination is of course relative, since the various radial shifts are computed by arbitrarily taking the first profile as a reference profile. To compute the radial

shifts, we limit ourselves to the range from $a = 132320$ km to $a = 132440$ km, where the phase is well-behaved and little affected by boundary effects. The phases agree to a few percent in the range from $a = 132320$ km to $a = 132440$ km, which we consider a very good result.

The radial shifts (or more precisely “unshifts”) in the semi-major axis (or radius) just determined must be accompanied by similar unshifts of τ_0 and q , f , and of the data themselves. This requires some interpolation over an interval in semi-major axis between 132270 km and 132440 km.

4.5 Recovery of the secondary parameters: mean solution construction

We are now in position to use the functions $\tau_0(a)$, $q(a)$, and $f(a)$ for each of the eight profiles to produce a single function for each quantity that should be valid for all eight profiles. In other words, we want to determine the mean solution for the functions τ_0 , q , and f . We treat each of these three functions separately.

It turns out that a polynomial fit to a simple average of each function on each point does not satisfactorily represent the true function (*i.e.*, the function used to generate the simulated profiles). Instead, we found that the following least square procedure yields good results. The variables of this fit are the mean values of the function over a limited number of points or nodes (we chose 10 for this wave) approximately regularly spaced between 132270 km and 132440 km, a range of values determined empirically to avoid edge effects. These variables are first estimated as the average values of the eight functions at each node, providing initial conditions to the least square fit. The function we wish to fit is computed everywhere by interpolation over these 10 values, and is constrained to best represent, in the least square sense, the set of eight profile-dependent functions between 132270 km and 132440 km. In order to avoid negative, unrealistic values of q , this quantity is constrained to a small, positive value at the resonance radius. This somewhat artificially constrains the behavior of q in the first wavelength. The negative values of q derived from the various profiles arise in part from the failure of the WKBJ approximation.

Figure 3 shows the mean solution in red for τ_0 , q , and $(f - f_{injected})/(2\pi)$, on the six upper panels. The left panels correspond to the case of data without noise, while the right panels correspond to noisy data. The green lines refer to the injected simulation parameters (*i.e.* the wave parameters used to generate the simulated data and shown in Fig. 2). The blue lines show the values determined independently for each profile. All the plots in the six upper panels are cut at 132270 and 132440 km because the failing of the WKJB approximation at the beginning of the wave and boundary effects near the end of the data set make the solution unreliable outside these cut-off values. As a matter of fact, the solution is incorrect within the first 50 km of the wave, where the wave function f is not determined accurately. As expected, there is more scatter in the case with noise than in the case without noise. Nevertheless, the agreement between the mean solution and the injected values between 132310 and 132440 km is remarkable. This illustrates the efficacy of this approach to find the mean solution for τ_0 , q , and f . The four lower panels will be discussed in the next section.

The improvement that this method brings to the determination of τ_0 and q , as compared to the individual determinations, can be quantified by looking at Fig. 6. The left panels are for the case

without noise and the right panels for the noisy data. The top panel of this figure pertains to τ_0 and the bottom panel pertains to q . The middle panels will be discussed in section 4.8. In each panel, the magenta lines display the function used to generate the simulated profiles (or injected function). The green and cyan lines show the minimum and maximum values F_{min} and F_{max} , respectively, of the computed $F = \tau_0$ or $F = q$ at any semi-major axis for the eight profiles. The red lines represent the mean solutions computed in this section. The black areas represent one standard deviation error bars computed as (the “noise” is statistically independent in the various profiles):

$$\sigma_F = \frac{(F_{max} - F_{min})}{2\sqrt{N_{PROF}}}, \quad (34)$$

where $N_{PROF} = 8$ is the number of profiles. We see that for both τ_0 and q , the magenta lines, which represent the true solutions, fall within the error bar areas, and most of the time coincide with the mean solutions, shown in red. Therefore Eq. (34) provides a reliable handle of the error on τ_0 and q . Also this figure demonstrates the need to have as many profiles as possible (preferably well distributed in $m\phi$) to compute accurately τ_0 and q . A precise determination of these parameters is especially important to determine the ring surface density and to constrain the ring stress tensor, which will be done in a future paper.

4.6 Recovery of the primary parameters: determination of ae and γ

To solve for ae and γ , we solve iteratively Eqs. (14) and (15), a procedure described in appendix A.2. The equations are solved between semi-major axes of 132290 km and 132440 km, as this iteration procedure involved in the resolution relies on the WKB approximation, which is not robust enough in the inner wave region. Where needed in other subsequent passes, ae and γ are linearly extrapolated outside the range specified above. This extrapolation is certainly one major source of error in this reconstruction procedure, which explains the relatively large (albeit tamed) difference between the injected and reconstructed phase functions within the first wavelength region. Improvement is clearly required on this point. This is discussed further in our last section.

Figure 3 shows the mean solution in red for ae and $\gamma - \pi/2$, on the four lower panels. As mentioned above, the left panels correspond to the case of data without noise, while the right panels correspond to noisy data. The green lines refer to the injected simulation parameters. We find a remarkable agreement between the mean solution and the injected values over most of the wave. There is a difference in the first 50 or 60 km of the wave, where the phase function was not well determined due to the failure of the WKB approximation.

4.7 Profiles reconstruction, and second correction to the radial scale

We are now in position to construct optical depth profiles $\tau(r, \phi) = \tau(a(r), \phi)$ over the entire radial range of the eight profiles, to check our obtained kinematic solution. We use Eqs. (11) and (24). In doing so, we determine by least squares a second approximation to the radial shifts required by the inconsistent absolute radial scale of the various profiles and the various approximations made

in the procedure. As before, this second shift translates into a correlative shift of all our kinematic functions. The final radial shifts are shown in Tables 1. The differences between the applied and the computed data shifts are in general significantly smaller in the absence of noise but even with noisy data, they amount to at most several tens of meters, which is much smaller than 250 m, the separation between the data points.

Figures 4 and 5 show the unshifted reconstructed profiles (in red) together with the unshifted simulated data (in blue) for the profiles without (left panels) and with noise (right panels). We can see that the agreement is excellent, and suggests that a better determination of the radial scale shifts is hardly possible. Note that the fit is still tamed inside the first wavelength region, although the reconstruction of ae , γ , and $m\Delta$ is only correct within a factor of two in this region. Nevertheless, an improved determination of the kinematic parameters will be required in this region to compute satellite torques with some accuracy. The very last peaks are not accurately represented because the fit was not performed in this region; the reconstructed parameters have simply been extrapolated there.

4.8 Recovery of the surface density

Recovering the surface density requires some further dynamical input, which is usually provided by the dispersion relation. As the effect of the ring stress tensor is small, the pressure correction is usually neglected in front of the self-gravity term in the dispersion relation, which then reduces to the following form in the region of validity of the WKBJ ordering:

$$K = \frac{2\pi GC(q)k\tau_0 a_{res}}{3(m-1)\Omega^2(a-a_{res})}, \quad (35)$$

where $K = \tau_0/\Sigma_0$ is the opacity. This expression was applied in the construction of our simulated data. The situation with real waves is more complex. Sremcevic et al. (2008) have argued that the pressure term leads to measurable changes in the dispersion on the order of 5%. For our application to the Mimas 5:3 density wave, we have taken this term into account [see Eq. (39)].

The opacity is the quantity we chose to recover, as the optical depth τ_o , the nonlinearity parameter, and the wavenumber k are known from the inversion procedure; k is computed as the derivative with respect to the semi-major axis of the phase function f .

We also make use of the error estimates on τ_o and q to estimate the error on the recovery of the opacity K and the surface density Σ_o . In doing so, we can neglect the error in k because the error in the slope of f is smaller than the error in f , leading to relative errors on k of the order of one or two percent at most, much smaller than the error in the two other quantities (of the order of 10 to 20%).

We have found that the deviations in q and τ_o of any given profile with respect to the mean are not independent, but rather tend to be anti-correlated. Therefore, they were not added. Instead, we computed K for five different cases, involving several combinations of τ_0 and q . Remember (see section 4.5) that we denote by $\tau_{0,min}$ (or q_{min}) and $\tau_{0,max}$ (or q_{max}) the minimum and maximum values of τ_0 (or q) in each data point computed independently for each profile. We denote by $\bar{\tau}_0$ and \bar{q} the mean values of τ_0 and q computed in section 4.5.

The values of the opacity are shown in the medium panels of Fig. 6. The left side corresponds to the data without noise, and the right side to the noisy data. The nominal value of the opacity, $K(\bar{\tau}_0, \bar{q})$ is displayed in red while the injected value of $K = 0.0125$ is plotted in magenta. In the second panels from the top, the green lines show $K(\tau_{0,min}, \bar{q})$ and the cyan lines show $K(\tau_{0,max}, \bar{q})$. In the third panels from the top, the green lines show $K(\bar{\tau}_0, q_{min})$ and the cyan lines show $K(\bar{\tau}_0, q_{max})$. The error bars, drawn in black, are computed by an equation similar to Eq. (34). One can see that the true solution (magenta), stays in the error bar area of the nominal solution between 60 and 170 km of the beginning of the wave. This demonstrates that the procedure leads to a much better solution than that could be inferred by considering the green and cyan lines, and that the black area (one standard deviation) gives an accurate estimate of the reconstruction error of the opacity.

The surface density can now be recovered easily as $\Sigma_0 = \tau_0/K$. It is plotted with red lines on Fig. 7. The top panel is for the case without noise and the bottom panel is for the case of the noisy data. The green lines represents the injected value.

We compared our background surface density with what would be predicted by the linear theory for each profile independently. For each profile, we determined k as the derivative of the profile phase ψ [see Eq. (22)], and we computed a constant background surface density by a least-squares fit of the equation:

$$\frac{a - a_{res}}{a_{res}\Sigma_0} = \frac{2\pi Gk}{3(m-1)\Omega^2}, \quad (36)$$

which is the linear dispersion relation. This is similar to what is routinely done in the literature.

The resulting values of Σ_0 for each profile are displayed as blue lines on the two panels. These values are above the average of the values obtained by using the nonlinear theory with our procedure. Fig. 7 clearly demonstrates the crudeness of the linear theory when the surface density is not constant, which is expected in real waves (see section 3). Our ultimate goal requires that we recover the variation of the surface density in the wave region; this makes the use of a procedure of reconstruction of the wave kinematics such as the one presented here a necessary first step.

5 Application to the Mimas 5:3 density wave

The application of our procedure to the actual data collected for the Mimas 5:3 density wave raises a number of other difficulties. The first one is related to the variations in the orbital motion of Mimas. Table 2 lists the four resonance locations that can be associated with the position of Mimas during the four occultations which provide the eight profiles we have analyzed. For each date, we have fitted over a period of two days the epicyclic elements to the orbital data given by the SPICE kernel *sat267*, and then we have solved for the position of the resonance. We see that the resonance location varies by 2.6 km, i.e. a sizeable fraction of the (varying) wavelength, leading to potentially non-negligible modulations of the wave between various profiles. Two limiting cases can be considered: in the first, the wave reacts in a quasi-static way to the variation of the orbit of Mimas; in the other, the satellite orbital variations are fast compared to the time-scale of adjustment

of the wave. Orders of magnitude estimates of the density wave group velocity show that it is larger than the speed of variation of the resonance location, but only by a factor of a few: the group velocity $\pi G \Sigma / \kappa$ (Shu 1984) is approximately 20 or 30 km/year for the Mimas 5:3 density wave, while the semi-major axis of Mimas varies by 2 or 3 km with a period of 225 days (in addition to the ~ 70 year period due to the resonance with Tethys). Nevertheless, we deal with this difficulty by setting the resonance radius at 132301 km and assuming one can absorb any modulation of the wave in the radial shifts of the profiles, as our aim is more to illustrate the behavior of our reconstruction method than to derive precise quantitative results. We found empirically that the radially rescaled profiles obtained in this way are reasonably consistent with one another, indicating that any spatial and temporal modulation of the wave behavior remains mild enough, a conclusion consistent with the recent findings of Stewart and Sremcevic (2008).

The second difficulty, already mentioned in the introduction, is that self-gravity wakes cause the apparent background optical depth to vary with viewing geometry (Colwell et al. 2006; Hedman et al. 2007). We normalized the optical depths of the eight profiles as follows. First we determined the mean optical depth $\bar{\tau}_j$ for each profile in an apparently unperturbed region of 20 km inward of the Mimas 5:3 density wave (see Table 2); it appears that modulations in the mean optical depth are rather moderate. Thus, we computed the average τ_{ave} of the $\bar{\tau}_j$ and we multiplied the optical depth of each profile by $\tau_{ave} / \bar{\tau}_j$. Nevertheless, the justification of this procedure is unclear as we do not know if wakes inside the wave, if present, affect the optical depth in the same way as outside it. In any case, this is not a large effect, probably less important than the uncertainty related to the large intrinsic noise observed in the radio data.

Next, we applied our procedure to the optical depth data. Fig. 8 shows the data (in blue) and the reconstructed profiles (in red) after three passes. The agreement between the model and the data is very good, considering the large fluctuations of the optical depth (notably at the peaks) present in the data. Fig. 9 is the equivalent of Fig. 3 with a few differences. In the absence of injected value, the phase function is compared to the its mean solution. The dotted lines correspond to the region where the functions for at least one of the profiles were extrapolated. In this extrapolation region, the functions τ_0 and q increase. These functions are nearly constant between 50 and 120 km from the beginning of the wave (at 132301 km, the selected resonance radius). In this domain (132351 to 132421 km), the phase function f is very well determined. As expected, ae increases and then decreases to zero, and γ is very close to $\pi/2$. Table 2 lists the shifts found for the eight profiles (they are all positive, but this is only a coincidence).

Fig. 10 is the equivalent of Fig. 6 but does not show the minimum and maximum values that were used to compute the error bars, since they do not provide additional information. The plots were traced in the domain where we can most trust the solution, i.e., between 132350 km and 132420 km. As we have not tried to determine a position-dependent opacity from the data, the opacity is not shown in this plot.

Instead, the calculation of the opacity along with the velocity dispersion is illustrated by Fig. 11. This figure was constructed as follows. We wrote the nonlinear dispersion relation in the form:

$$g_{th} = g_{obs}, \quad (37)$$

with:

$$g_{obs} = \frac{2\pi G\alpha C(q)k\tau_0}{3(m-1)\Omega^2}, \quad (38)$$

$$g_{th} = \alpha K \left[\frac{(a - a_{res})}{a_{res}} - \frac{2k^2 H(q^2)c_0^2}{3(m-1)\Omega^2} \right], \quad (39)$$

where $\alpha = 1 \times 10^{12}$ is an ad hoc numerical factor designed to bring g_{obs} and g_{th} to values of order unity and a_{res} is the resonance semi-major axis. The second term in Eq. (39) is the pressure term, in the hydrodynamic approximation where the (vertically integrated) pressure is given by a simple isothermal equation of state $p = \Sigma c_0^2$; it introduces the isothermal sound speed (of the order of the particles' velocity dispersion) c_0 as a second parameter besides the opacity in the dispersion relation. Indeed, we found that the data were good enough to allow us to account for the pressure correction to the dispersion relation, which leads to a better agreement between g_{th} and g_{obs} . At this point, it is unclear if the remaining deviations from the purely self-gravitational term are due to imperfection in the radio data that would intrinsically bias the determination of q and τ_0 (a point further discussed below), imperfections in the model of the pressure term, neglect of the satellite term, or position dependence of the opacity and velocity dispersion; note in any case that Longaretti and Borderies (1986) pointed out that a constant opacity provided a better fit to the dispersion relation than a constant surface density.

We chose to determine only the opacity and velocity dispersion, and not the resonance radius, for reasons also discussed below. We find the velocity dispersion c_0 and the opacity K by a least-squares fit of Eq. (37) over the interval between 50 and 120 km from the beginning of the wave, in the following way.

In Fig. 11, the solid lines represent the values of:

$$g_1 = \alpha K \frac{(a - a_{res})}{a_{res}}, \quad (40)$$

and the dashed lines represent the values of:

$$g_2 = \frac{2\alpha\pi G\tau_0 k C(q)}{3(m-1)\Omega^2} - \frac{2\alpha k^2 H(q^2)c_0^2 K}{3(m-1)\Omega^2}. \quad (41)$$

The black lines were obtained by using the mean values of τ_0 and q . The red and blue lines on the top panel were obtained by using the mean value of τ_0 and the minimum and maximum values of q provided by the error bars on this variable. On the other hand the red and blue lines on the bottom panel were obtained by using the mean value of q and the minimum and maximum values of τ_0 provided by the error bars on this variable (one standard deviation). These error bars indicate that deviations from strict linearity may be real; this point will be further investigated elsewhere. In the nominal case, the solution gives $c_0 = 0.55$ cm/s and $K = 0.018$ cm²/g.

Because of the non-constant background optical depth, the constant opacity results in a non-constant surface density, shown in red in Fig. 12. The blue lines were obtained for the use of the dispersion relation in the linear limit ($q \ll 1$). Note that we have $C(q)\Sigma_{0,NL} \Sigma_{0,L}$ where the subscripts NL and L refer to nonlinear and linear, respectively. Since $C(q) > 1$, we expect the

nonlinear background surface density to be smaller than the linear background surface density, as observed.

It is important to note that the cutoff of the radio data at an optical depth of about 5 for the profiles considered, due to the instrumental noise in the radio data, flattens the peaks to this value. This affects the determination of τ_0 and q . Also, the unexpectedly large fluctuations in optical depth observed at the wave peaks with respect to troughs lead to a similar systematic effect. Similarly, the noise level precludes a reliable determination of the weak peaks in the wave damping region, which is eventually needed to constrain the ring stress tensor. As mentioned earlier, we have verified that the errors in τ_0 and q are anti-correlated. Attempts to fit Eq. (37) with other combinations of τ_0 and q led to the result that the best estimate of a_{res} was obtained for the minimum value of τ_0 and the maximum value of q . This indicated that τ_0 is overestimated and q is underestimated, and led us to enforce the position of the resonance in the fit. We conclude that the variations of the background optical depth and surface density and the variations of the nonlinearity parameter derived from the radio data are imperfectly determined from the radio data. A better determination, which could come from using optical occultation data, is needed to study the damping of the wave and extract more (and more reliable) information from the dispersion relation.

6 Conclusion

We have established a robust procedure to analyze nonlinear density waves and we have applied it to the Mimas 5:3 density wave. In principle, the number of independent profiles provided by the Cassini mission would seem to make it possible to devise an inversion procedure relying only on the kinematic characteristics of the wave, but we found that in practice, and relying only on the radio data, this fails for three major reasons: the differences in the absolute radial scales of different profiles, the complex way in which the $a(r)$ relation comes into play, and the sensitivity to errors in the dependence of the wave phase on semi-major axis.

Instead, we have extended and considerably improved the method introduced in Longaretti and Borderies (1986), which relies not only on the wave kinematics, but on the WKBJ ordering as well. The intrinsic nonlinearity of the problem makes the procedure complex. Nevertheless, it is possible to reconstruct the wave parameters as well as the data, in the presence of uncertainties in the absolute scale of about ± 2 km and of noise in the data; the data resolution adopted was 250 m but the results should not be sensitive to this parameter.

As such, this inversion procedure performs very well in the far wave region. This opens new possibilities of physical diagnostics of wave regions. In particular, with the help of the nonlinear dispersion relation and the wave damping equation, one may possibly constrain the surface density and ring's stress tensor in a joint way, which would provide us with an indirect window on the ring's collisional physics. We plan to make use of this inversion procedure to undertake such systematic studies in the future.

The major inaccuracy of this reconstruction procedure is its limited efficacy within the first wavelength of propagation of the wave, where the WKBJ ordering is expected to fail on theoretical grounds, an expectation confirmed by the behavior observed in actual wave profiles. This limitation

is most drastic in the reconstruction of the eccentricity $e(a)$ and lag angle $\Delta(a)$. This is unfortunate for the purpose of the determination of the exchange of angular momentum with the satellite, as the generic expression of the torque results from a radial integral involving these two quantities [see, e.g., Eq. (35) of Longaretti and Borderies 1986]. The results of the present inversion method (which yields a fairly educated guess of the form of the kinematic parameters even inside the first wavelength, and has allowed us to remove the problem of inconsistencies of the absolute radial scale between the various profiles), may ensure the convergence of a refined, direct inversion method of the type we initially tried, provided enough high quality profiles are available. This approach may require to a different method of inversion of Eqs. (14) and (15), if needed; a possible way to do this is to re-express these equations as a set of nonlinear algebraic equations, and solve them by an algebraic iteration method. Additionally, further dynamical constraints may be needed to ensure that such a direct inversion method is well-defined. Three levels of such constraints are available in the literature. In their most useful form, they are all related to the dynamical equation governing the behavior of $Z \equiv e \exp(im\Delta)$ (see Shu et al. 1985c): they are the dynamical equation itself, its solution in the linear limit, and the asymptotic behavior of this solution in the evanescent region. Defining the most appropriate strategy on this issue requires substantial additional work, which will be reported elsewhere.

The application to the actual data of the Mimas 5:3 density wave gives good results, although the determination of τ_0 and q is impaired by the noise in the radio data; better results are expected from the use of, e.g., the UVIS data.

A Appendix

A.1 Radius versus semi-major axis inversion procedure:

To compute the semi-major axis a as a function of the radius we make use of Eq. (11) in an iterative procedure. The $(n + 1)$ th approximation of a , denoted $a^{(n+1)}$, is related to the n th one through

$$a^{(n+1)} = r + a^{(n)} e(a^{(n)}) \cos[m\phi + m\Delta(a^{(n)})]. \quad (42)$$

Convergence is ensured because $e \ll 1$; the procedure is initialized with $a^{(0)} = r$.

The reader may ask why Eq. (11) cannot be analytically inverted, at least approximately. This would be a definite advantage in the numerical implementation of our procedure, as the previous inversion is quite heavily required, and slows down the whole process. In principle, one could do this through an expansion in eccentricity. The zeroth order solution is:

$$a = r + r e(r) \cos(m\phi + m\Delta(r)). \quad (43)$$

We look for the first order solution by writing $a = r + \delta_1$ with $\delta_1 = \mathcal{O}(e)$. We find:

$$\delta_1 = \frac{r e(r) \cos(m\phi + m\Delta(r))}{1 - q(r) \cos \psi(r)}. \quad (44)$$

The second order solution is of the form $a = r + \delta_1 + \delta_2$ with:

$$\delta_2 = \frac{1}{2} \frac{[re(r) \cos(m\phi + m\Delta(r))]^2}{[1 - q(r) \cos \psi(r)]^3} \left[\frac{dq(r)}{dr} \cos \psi(r) - q \frac{d\psi(r)}{dr} \sin \psi(r) \right]. \quad (45)$$

Figure 13 shows the error between the approximate $a(r)$ obtained when using the zeroth, first, and second order solutions and the actual $a(r)$. Naturally, the actual functions $e(a)$ and $\Delta(a)$ (evaluated at $a = r$) are used in the process. Although the eccentricity is very small, the error is substantial, of order 1 km, and the convergence is very slow due to the various powers of the $1/J$ factors involved in this expansion, and more crucially due to the fact that the order of the k th order term in the expansion is not of magnitude e^k but $ae(ae/\xi)^{k-1}$, where ξ is the scale of variation of the wave amplitude introduced in section 2.2; the factor ae/ξ is substantially larger than e . This is why we adopted the iterative method described above.

However, using the same type of eccentricity expansion, one can check the statement made earlier about the impact of the $\theta = \phi$ assumption; the difference lies in the fact that in this case the expansion at order k is really of magnitude e^k .

A.2 Recovery of the primary kinematic paramaters

The approximate WKBJ ordering which applies over nearly all the wave propagation region suggests that Eqs. (14) and (15) can be used in an iterative way to determine e and γ . In practice, defining the n th order approximation of e and γ as $e^{(n)}$ and $\gamma^{(n)}$, we use:

$$ae^{(n)} = \frac{q \sin \gamma^{(n)}}{[df/da - d\gamma^{(n)}/da]}, \quad (46)$$

and

$$\cos \gamma^{(n+1)} = \frac{1}{q} \frac{dae^{(n)}}{da}. \quad (47)$$

Note that these equations are used alternatively and not simultaneously: $\gamma^{(n)}$ gives $e^{(n)}$ from Eq. (46), and $e^{(n)}$ in turn gives $\gamma^{(n+1)}$ from Eq. (47). The iteration is started with $\gamma^{(0)} = \pi/2$. Obviously, this fails inside the first wavelength, as convergence is ensured only when γ is not substantially different from $\pi/2$.

These expressions involve derivatives of f and γ with respect to a . We compute these derivatives by using a degree 5 polynomial interpolation of f and a simple procedure for the derivatives of ae and γ . Furthermore, we must smooth ae and γ after each iteration in order to avoid propagation of numerical noise through successive numerical derivatives. We stop the iteration process when the results become stable.

ACKNOWLEDGMENTS:

The research described in this publication was carried out at the Jet Propulsion Laboratory, California Institute of Technology, under a contract with the National Aeronautics and Space Administration. We are very grateful to Drs. M. Tiscareno and J. Colwell for their careful reviews of the manuscript and excellent suggestions.

References

- N. Borderies and P. Y. Longaretti. Description and behavior of streamlines in planetary rings. *Icarus*, 72:593–603, December 1987.
- N. Borderies, P. Goldreich, and S. Tremaine. Perturbed particle disks. *Icarus*, 55:124–132, July 1983.
- N. Borderies, P. Goldreich, and S. Tremaine. A granular flow model for dense planetary rings. *Icarus*, 63:406–420, September 1985.
- N. Borderies, P. Goldreich, and S. Tremaine. Nonlinear density waves in planetary rings. *Icarus*, 68:522–533, December 1986.
- N. Borderies-Rappaport and P.-Y. Longaretti. Test particle motion around an oblate planet. *Icarus*, 107:129–141, January 1994.
- J. E. Colwell and L. W. Esposito. Density and Bending Waves in Saturn’s Rings from Cassini UVIS Star Occultations. In *AAS/Division for Planetary Sciences Meeting Abstracts*, volume 39 of *AAS/Division for Planetary Sciences Meeting Abstracts*, page 26.06, October 2007.
- J. E. Colwell, L. W. Esposito, and M. Sremčević. Self-gravity wakes in Saturn’s A ring measured by stellar occultations from Cassini. *Geophys. Res. Lett.*, 33:7201, April 2006.
- J. E. Colwell, L. W. Esposito, M. Sremčević, G. R. Stewart, and W. E. McClintock. Self-gravity wakes and radial structure of Saturn’s B ring. *Icarus*, 190:127–144, September 2007.
- R. G. French, P. D. Nicholson, M. L. Cooke, J. L. Elliot, K. Matthews, O. Perkovic, E. Tollestrup, P. Harvey, N. J. Chanover, M. A. Clark, E. W. Dunham, W. Forrest, J. Harrington, J. Pipher, A. Brahic, I. Grenier, F. Roques, and M. Arndt. Geometry of the Saturn system from the 3 July 1989 occultation of 28 SGR and Voyager observations. *Icarus*, 103:163–214, June 1993.
- P. Goldreich and S. Tremaine. The dynamics of planetary rings. *Ann. Rev. Astron. Astrophys.*, 20:249–283, 1982.
- M. M. Hedman, P. D. Nicholson, H. Salo, B. D. Wallis, B. J. Buratti, K. H. Baines, R. H. Brown, and R. N. Clark. Self-Gravity Wake Structures in Saturn’s A Ring Revealed by Cassini VIMS. *Astron. J.*, 133:2624–2629, June 2007.

- R. A. Jacobson, P. G. Antreasian, J. J. Bordi, K. E. Criddle, R. Ionasescu, J. B. Jones, R. A. Mackenzie, M. C. Meek, D. Parcher, F. J. Pelletier, W. M. Owen, Jr., D. C. Roth, I. M. Roundhill, and J. R. Stauch. The Gravity Field of the Saturnian System from Satellite Observations and Spacecraft Tracking Data. *Astron. J.*, 132:2520–2526, December 2006.
- R. Karjalainen and H. Salo. Gravitational accretion of particles in Saturn’s rings. *Icarus*, 172: 328–348, 2004.
- A. J. Kliore, J. D. Anderson, J. W. Armstrong, S. W. Asmar, C. L. Hamilton, N. J. Rappaport, H. D. Wahlquist, R. Ambrosini, F. M. Flasar, R. G. French, L. Iess, E. A. Marouf, and A. F. Nagy. Cassini Radio Science. *Space Science Reviews*, 115:1–70, December 2004.
- M. C. Lewis and G. R. Stewart. Effects of Self-Gravity on Wakes at the Encke Gap. In *Bulletin of the American Astronomical Society*, pages 1089–+, October 2000.
- M. C. Lewis and G. R. Stewart. Expectations for Cassini observations of ring material with nearby moons. *Icarus*, 178:124–143, November 2005.
- P. Longaretti. Planetary Ring Dynamics: from Boltzmann’s Equation to Celestial Mechanics. In D. Benest and C. Froeschle, editors, *Interrelations Between Physics and Dynamics for Minor Bodies in the Solar System*, pages 453–+, 1992.
- P.-Y. Longaretti. Saturn’s main ring particle size distribution - an analytic approach. *Icarus*, 81: 51–73, 1989.
- P.-Y. Longaretti and N. Borderies. Nonlinear study of the Mimas 5:3 density wave. *Icarus*, 67: 211–223, August 1986.
- P.-Y. Longaretti and N. Borderies. Streamline formalism and ring orbit determination. *Icarus*, 94: 165–170, November 1991.
- E. A. Marouf, G. L. Tyler, and P. A. Rosen. Profiling Saturn’s rings by radio occultation. *Icarus*, 68:120–166, October 1986.
- P. D. Nicholson, M. L. Cooke, and E. Pelton. An absolute radius scale for Saturn’s rings. *Astron. J.*, 100:1339–1362, October 1990.
- P. D. Nicholson, M. M. Hedman, R. N. Clark, M. R. Showalter, D. P. Cruikshank, J. N. Cuzzi, G. Filacchione, F. Capaccioni, P. Cerroni, G. B. Hansen, B. Sicardy, P. Drossart, R. H. Brown, B. J. Buratti, K. H. Baines, and A. Coradini. A close look at Saturn’s rings with Cassini VIMS. *Icarus*, 193:182–212, January 2008.
- P. A. Rosen, G. L. Tyler, and E. A. Marouf. Resonance structures in Saturn’s rings probed by radio occultation. I - Methods and examples. *Icarus*, 93:3–24, September 1991a.
- P. A. Rosen, G. L. Tyler, E. A. Marouf, and J. J. Lissauer. Resonance structures in Saturn’s rings probed by radio occultation. II - Results and interpretation. *Icarus*, 93:25–44, September 1991b.

- M. R. Showalter and P. D. Nicholson. Saturn's rings through a microscope - Particle size constraints from the Voyager PPS scan. *Icarus*, 87:285–306, October 1990.
- F. H. Shu. Waves in planetary rings. In R. Greenberg and A. Brahic, editors, *Planetary Rings*, pages 513–561, 1984.
- F. H. Shu, L. Dones, J. J. Lissauer, C. Yuan, and J. N. Cuzzi. Nonlinear spiral density waves - Viscous damping. *Astrophys. J.*, 299:542–573, December 1985a.
- F. H. Shu, L. Dones, J. J. Lissauer, C. Yuan, and J. N. Cuzzi. Nonlinear spiral density waves - Viscous damping. *Astrophys. J.*, 299:542–573, December 1985b.
- F. H. Shu, C. Yuan, and J. J. Lissauer. Nonlinear spiral density waves - an inviscid theory. *Astrophys. J.*, 291:356–376, April 1985c.
- L. J. Spilker, S. Pilorz, A. L. Lane, R. M. Nelson, B. Pollard, and C. T. Russell. Saturn A ring surface mass densities from spiral density wave dispersion behavior. *Icarus*, 171:372–390, October 2004.
- M. Sremcevic, G. R. Stewart, N. Albers, J. E. Colwell, and L. W. Esposito. Density Waves in Saturn's Rings: Non-linear Dispersion and Moon Libration Effects. In *AAS/Division of Dynamical Astronomy Meeting*, volume 39, page #18.05, May 2008.
- G. R. Stewart and M. Sremcevic. Temporally Modulated Density Waves in Saturn's Rings. In *AAS/Division of Dynamical Astronomy Meeting*, volume 39, page #18.06, May 2008.
- M. S. Tiscareno, P. D. Nicholson, J. A. Burns, M. M. Hedman, and C. C. Porco. Unravelling Temporal Variability in Saturn's Spiral Density Waves: Results and Predictions. *Astrophys. J. Lett.*, 651:L65–L68, November 2006.
- M. S. Tiscareno, J. A. Burns, P. D. Nicholson, M. M. Hedman, and C. C. Porco. Cassini imaging of Saturn's rings II. A wavelet technique for analysis of density waves and other radial structure in the rings. *Icarus*, 189:14–34, July 2007.
- S. J. Weidenschilling, C. R. Chapman, D. R. Davis, and R. Greenberg. Ring particles - Collisional interactions and physical nature. In R. Greenberg and A. Brahic, editors, *Planetary Rings. Univ. Arizona*, pages 367–415, 1984.
- H. A. Zebker, E. A. Marouf, and G. L. Tyler. Saturn's rings - Particle size distributions for thin layer model. *Icarus*, 64, December 1985.

Profile #	1	2	3	4	5	6	7	8
$m\phi$	-29.477	-160.081	176.166	44.460	122.805	16.740	60.007	-9.538
Applied shifts (km)	0	-0.5	-1.0	0.5	1.0	-1.0	-1.5	1.5
Computed shifts (km)	0	-0.500	-1.001	0.502	1.002	-0.980	-1.441	1.501
Differences (m)	0	0	1	2	2	20	59	1
Applied shifts (km)	0	-0.5	-1.0	0.5	1.0	-1.0	-1.5	1.5
Computed shifts (km)	0	-0.519	-1.038	0.460	0.978	-1.009	-1.524	1.424
Differences (m)	0	19	38	40	22	9	24	76

Table 1: First line: Values of $m\phi$ ($m = 4$) in degrees for each of the eight profiles. Next three lines: Computed shifts of the simulated profiles without noise compared to the shifts applied in generating the simulated data without noise; absolute differences between the applied shifts and the computed shifts. Last three lines: Computed shifts of the noisy simulated profiles compared to the shifts applied in generating the simulated data; absolute differences between the applied shifts and the computed shifts.

Profile	Rev.	Date	a_{res}	$\bar{\tau}$	Radial shift
1	7	May 3, 2005	132301.717	0.84	0
2	7	May 3, 2005	132301.717	0.72	1.550
3	8	May 21, 2005	132302.037	0.78	0.564
4	8	May 21, 2005	132302.037	0.77	1.449
5	10	June 26, 2005	132300.601	0.72	0.361
6	10	June 26, 2005	132300.601	0.77	0.146
7	12	August 2, 2005	132299.480	0.72	0.830
8	12	August 2, 2005	132299.480	0.75	0.177

Table 2: Location a_{res} of the Mimas 5:3 resonance for the four dates of each profile. Each date has an ingress and an egress so we have eight profiles. Average optical depth $\bar{\tau}$ for each profile in an unperturbed region of 20 km inward of the Mimas 5:3 resonance. Radial shifts obtained by the procedure.

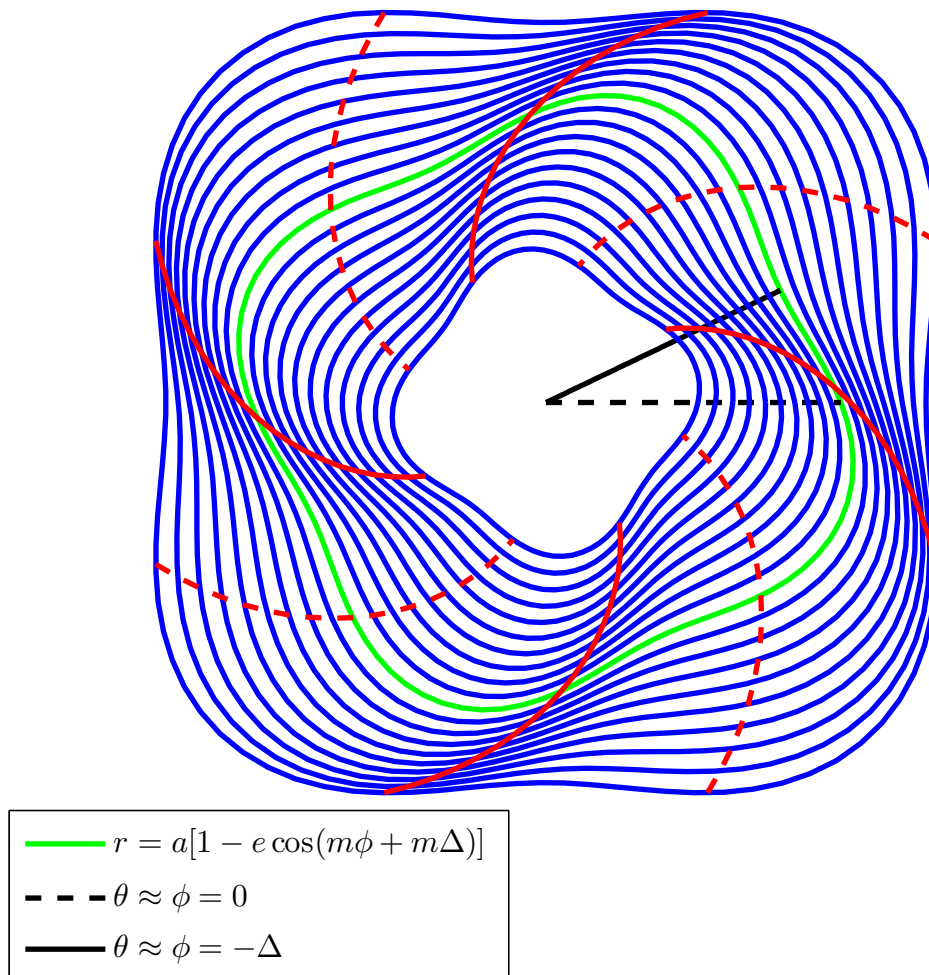


Figure 1: Streamlines of a 4-lobe ($m = 4$) density wave, such as Mimas 5:3. The lag angle Δ provides the relative shift in angle of one streamline to the next. The loci of constant profile phase ψ corresponding to the density maxima ($\psi = 2\pi n$ with $n = 1$ to 5, solid line) and minima ($\psi = \pi$ modulo 2π , dashed line) are also shown to illustrate the geometrical meaning of ψ . A streamline has been singled out, to show the phase angle Δ .

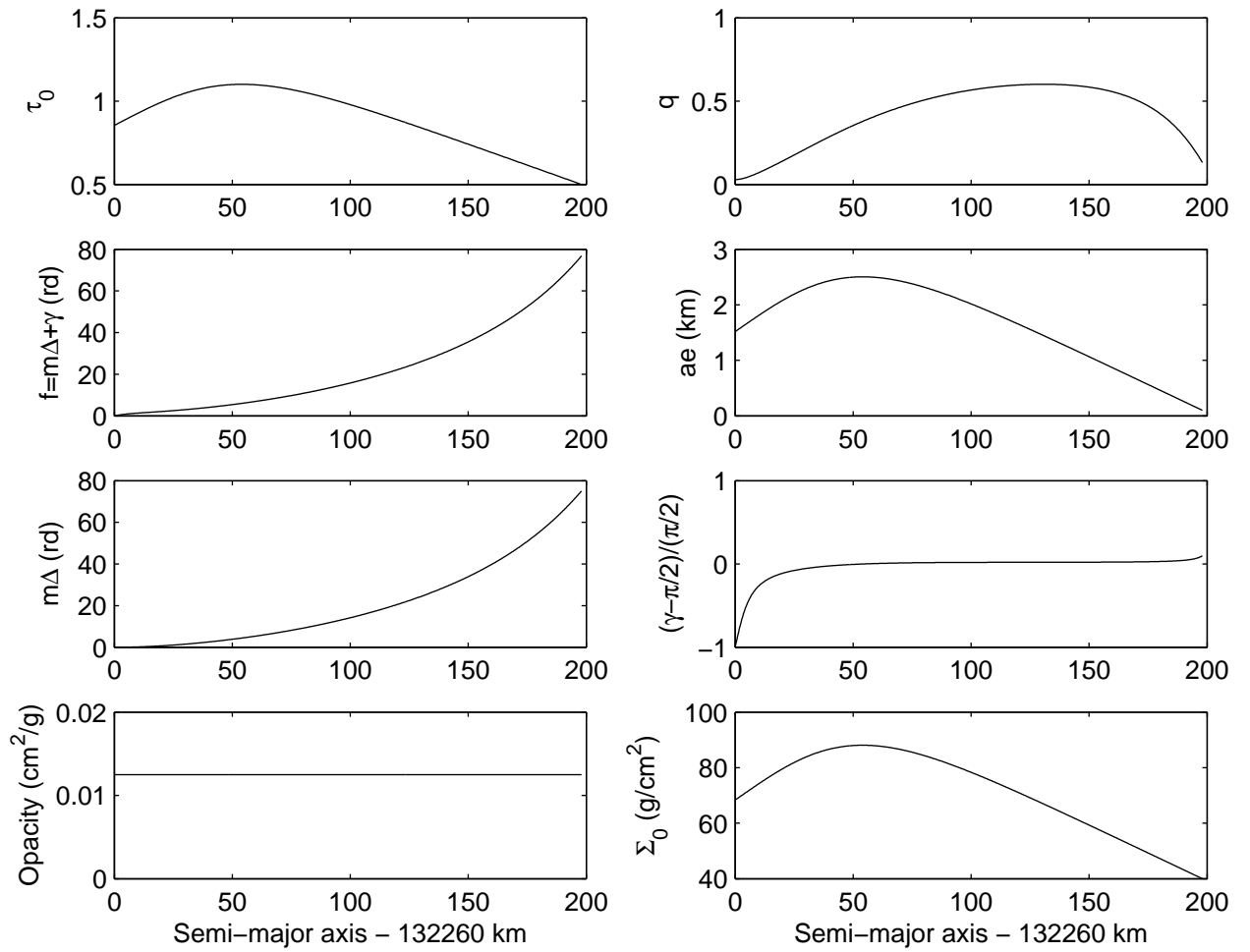


Figure 2: Kinematic wave parameters for the simulated profiles. These parameters were computed as described in section 3. The assumed resonance radius is 132260 km.

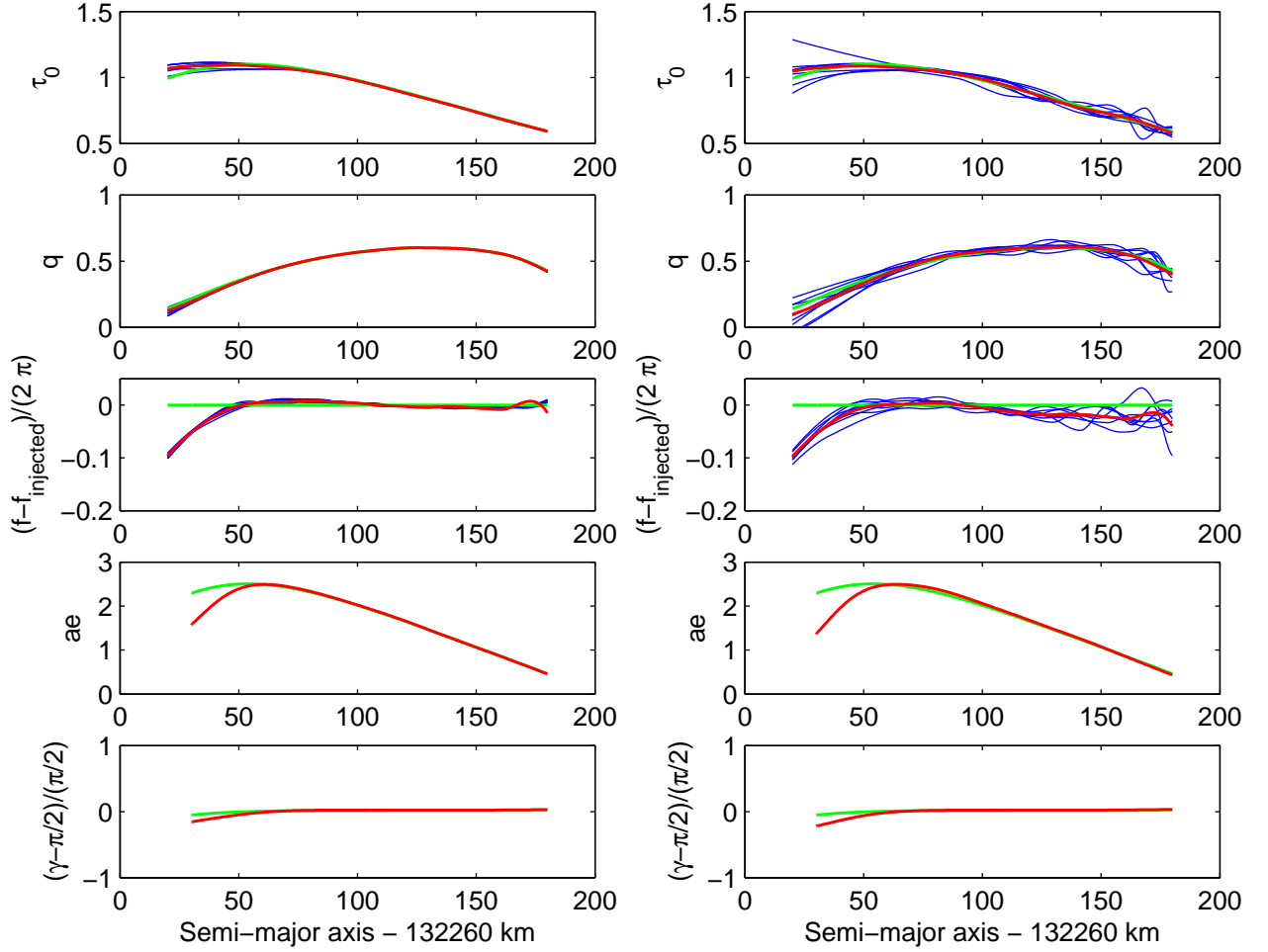


Figure 3: Solution for the five wave kinematic parameters after three passes for the simulation case without noise (left panels) and with noise (right panels). The blue lines show the solutions for the profiles taken independently from each other. The red lines display the mean solution. The green lines refer to the values injected in the simulation (see Fig. 2).

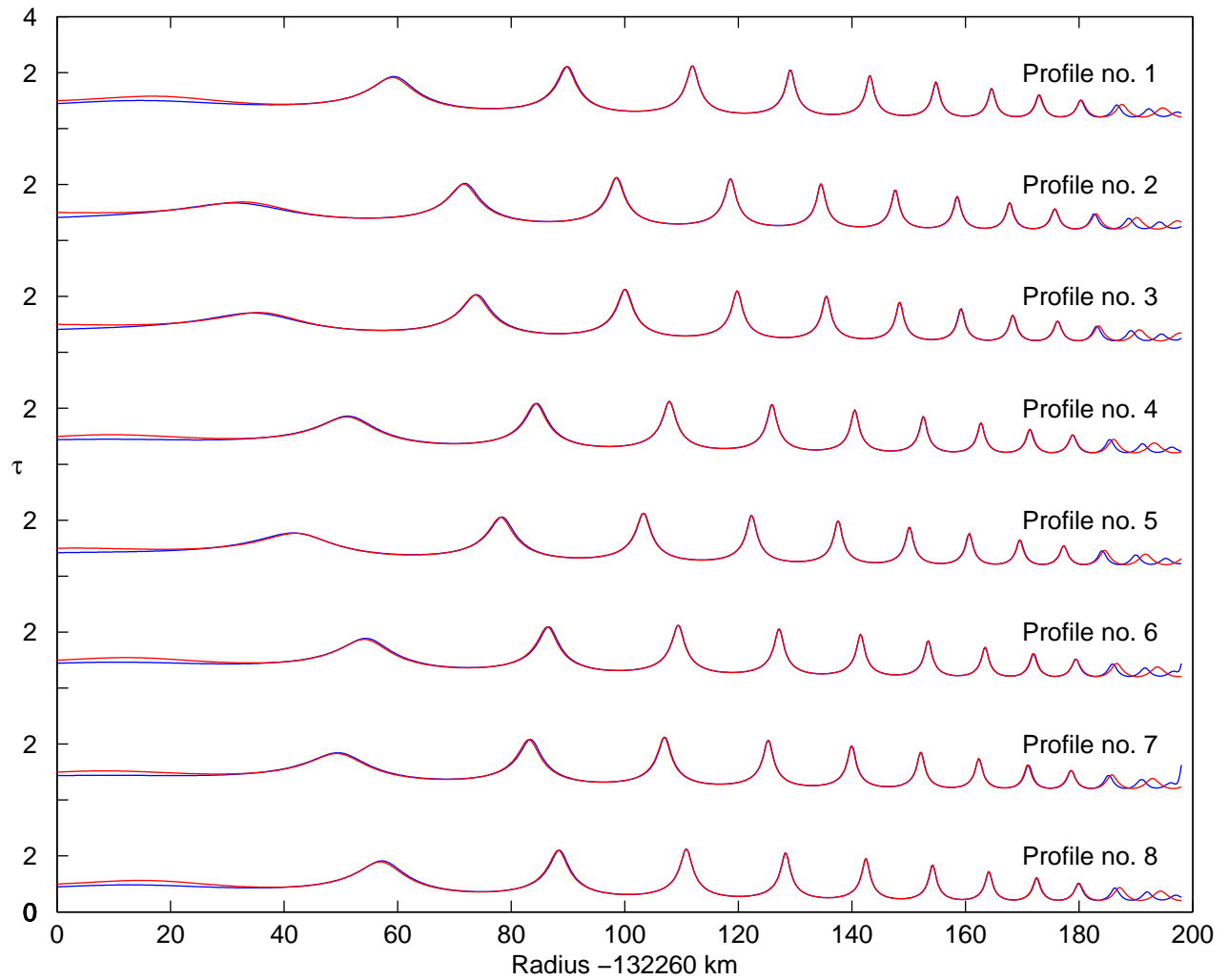


Figure 4: Simulated profiles in blue for the case without noise, and reconstructed profiles in red. For each profile, the optical depth scale varies between 0 and 4. Intermediate tick marks represent both the $\tau = 0$ level of the next profile, and the $\tau = 4$ level of the previous one.

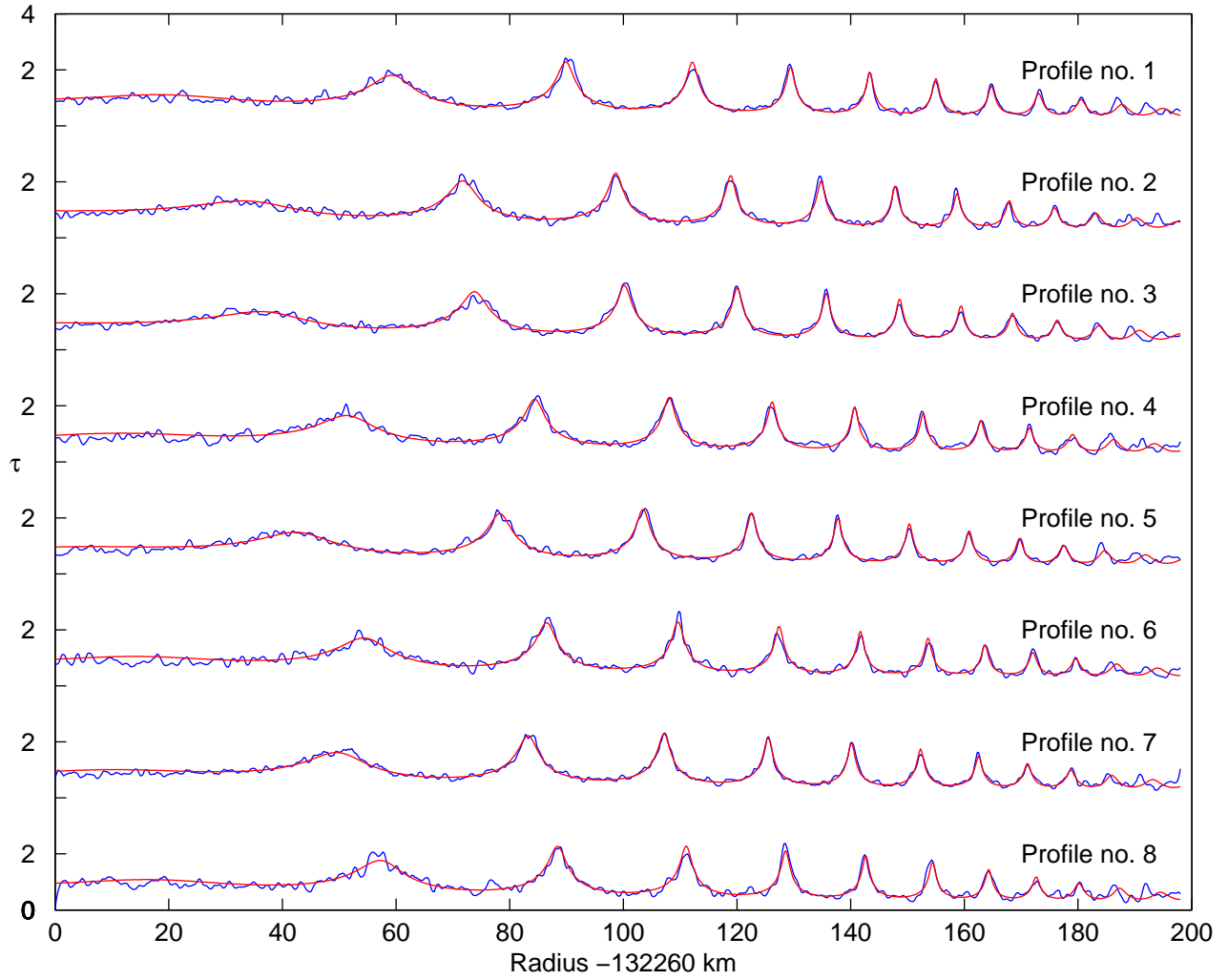


Figure 5: Simulated profiles in blue for the case with noise, and reconstructed profiles in red. For each profile, the optical depth scale varies between 0 and 4. Intermediate tick marks represent both the $\tau = 0$ level of the next profile, and the $\tau = 4$ level of the previous one.

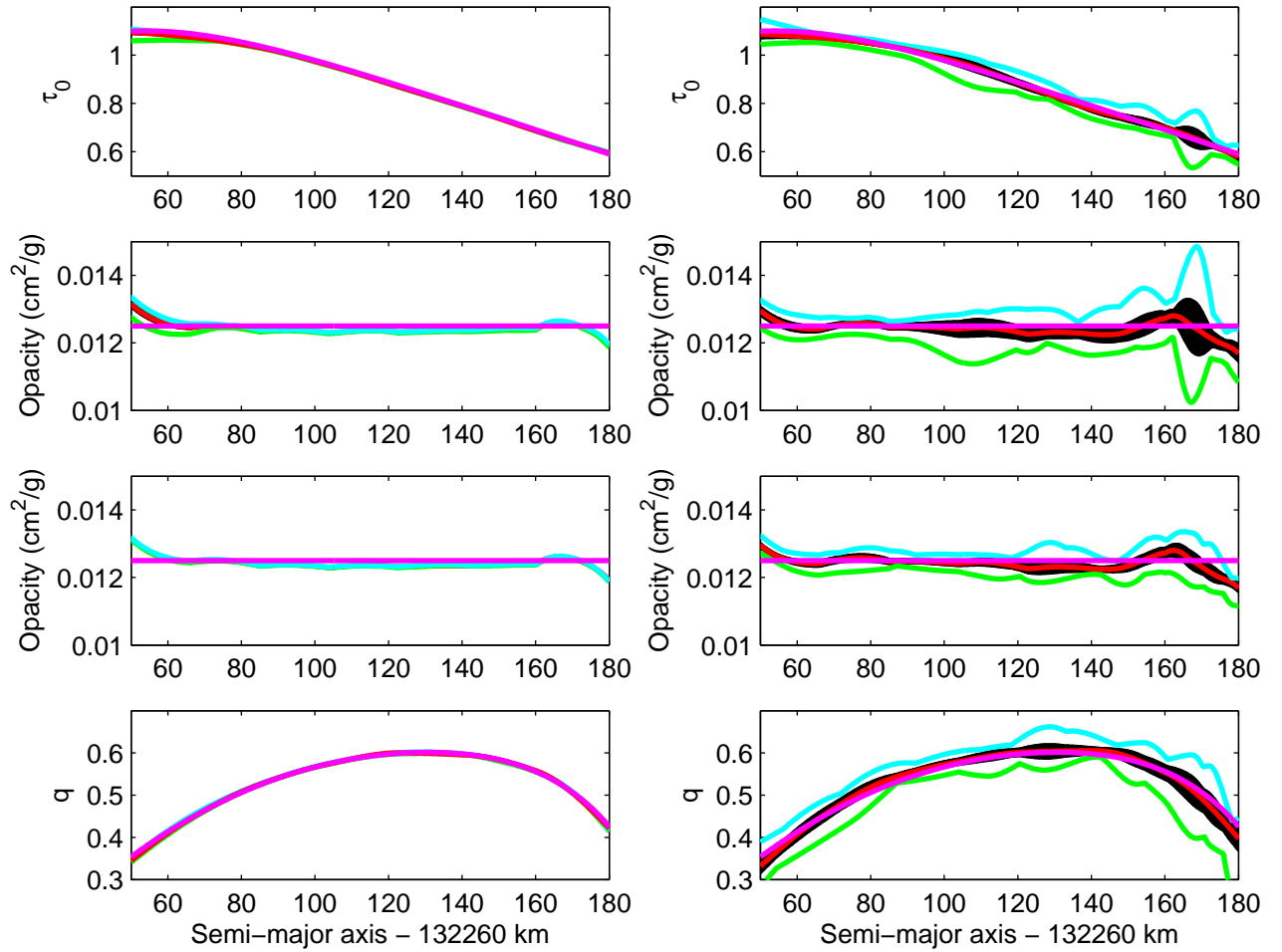


Figure 6: Background optical depth, opacity, and nonlinearity parameters for the simulated cases without noise (left panels) and the cases with noise (right panels). In each panel, the red line represents the solution, surrounded by its error bars in black. The injected values used to generate the simulated data are displayed by magenta lines. On the top and bottom panels, the green and cyan lines show the minimum and maximum values of the function obtained by analyzing the profiles independently of each other up to the point where a mean solution is determined. There are two panels for the opacity corresponding to two ways of computing the error bars (see section 4.8). This section also explains how the green and cyan lines were obtained.

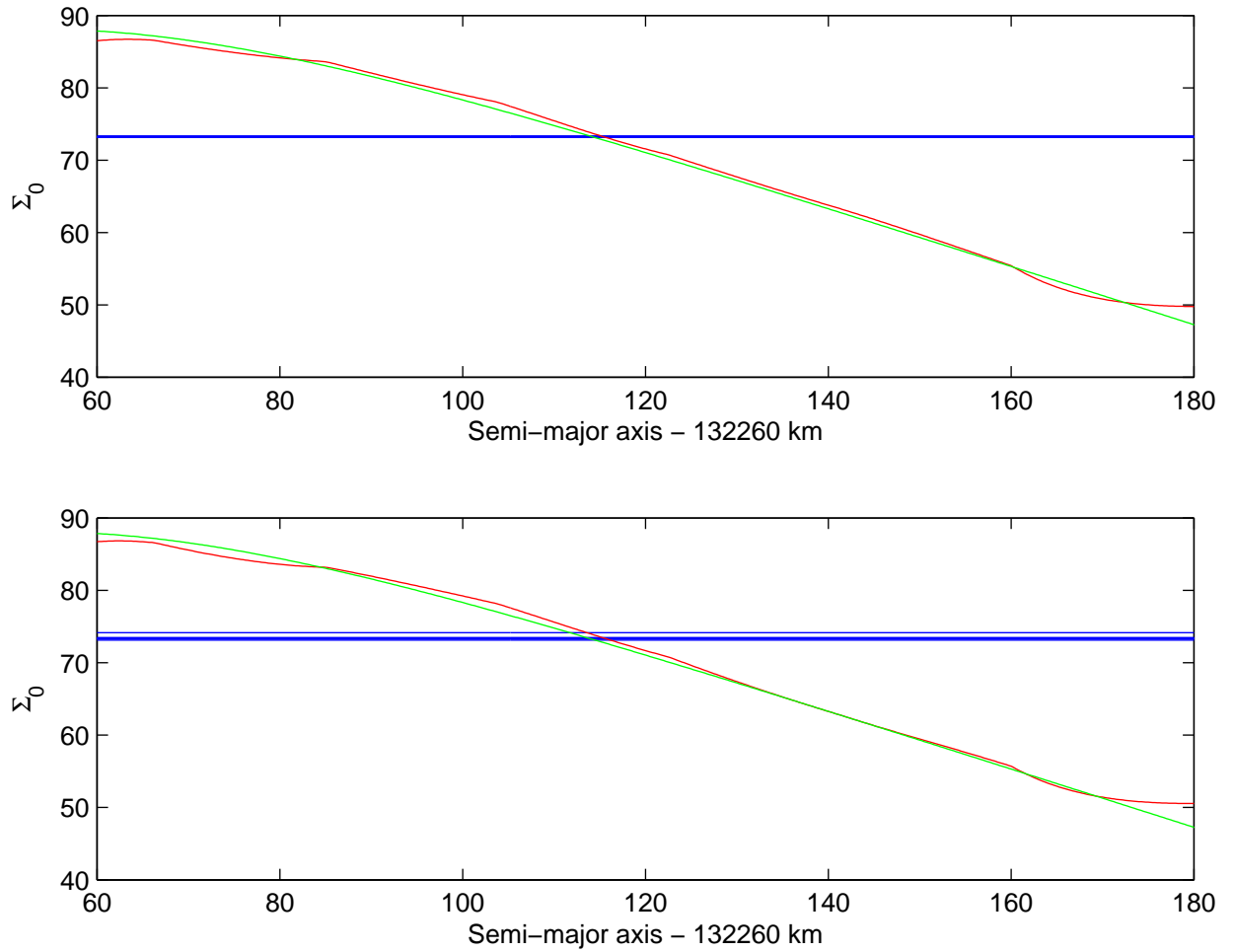


Figure 7: For the simulation, surface density computed by a fit to the linear theory (blue lines), computed by the nonlinear theory (red), and injected in the simulation (green). The top panel is for the case without noise, and the bottom panel is for the case with noise.

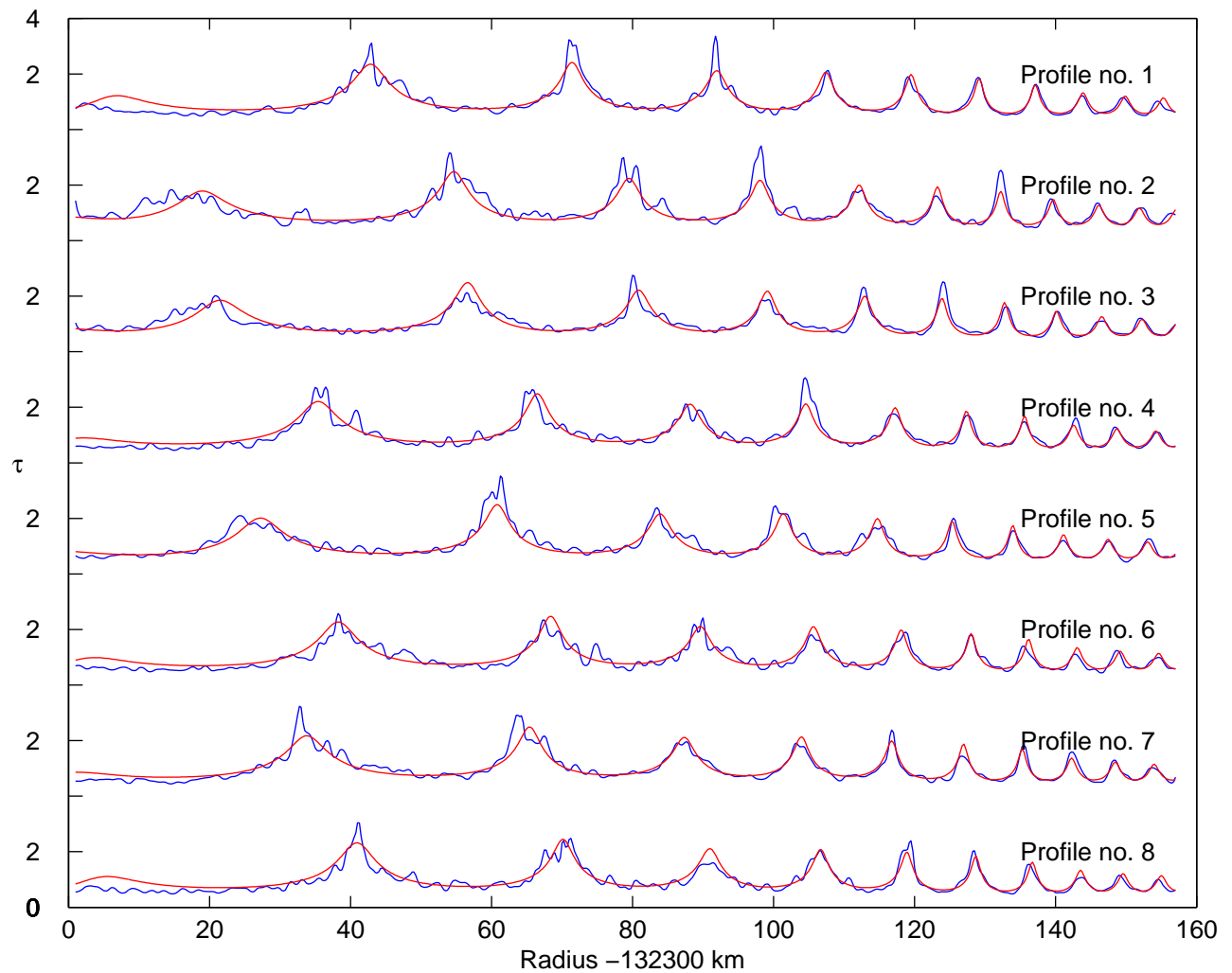


Figure 8: Radio optical depth profiles for eight occultations (in blue) of the Mimas 5:3 density wave and solution after three passes (in red). For each profile, the vertical scale goes from 0 to 4. Intermediate tick marks represent both the $\tau = 0$ level of the next profile, and the $\tau = 4$ level of the previous one. The resonance radius is 132301 km.

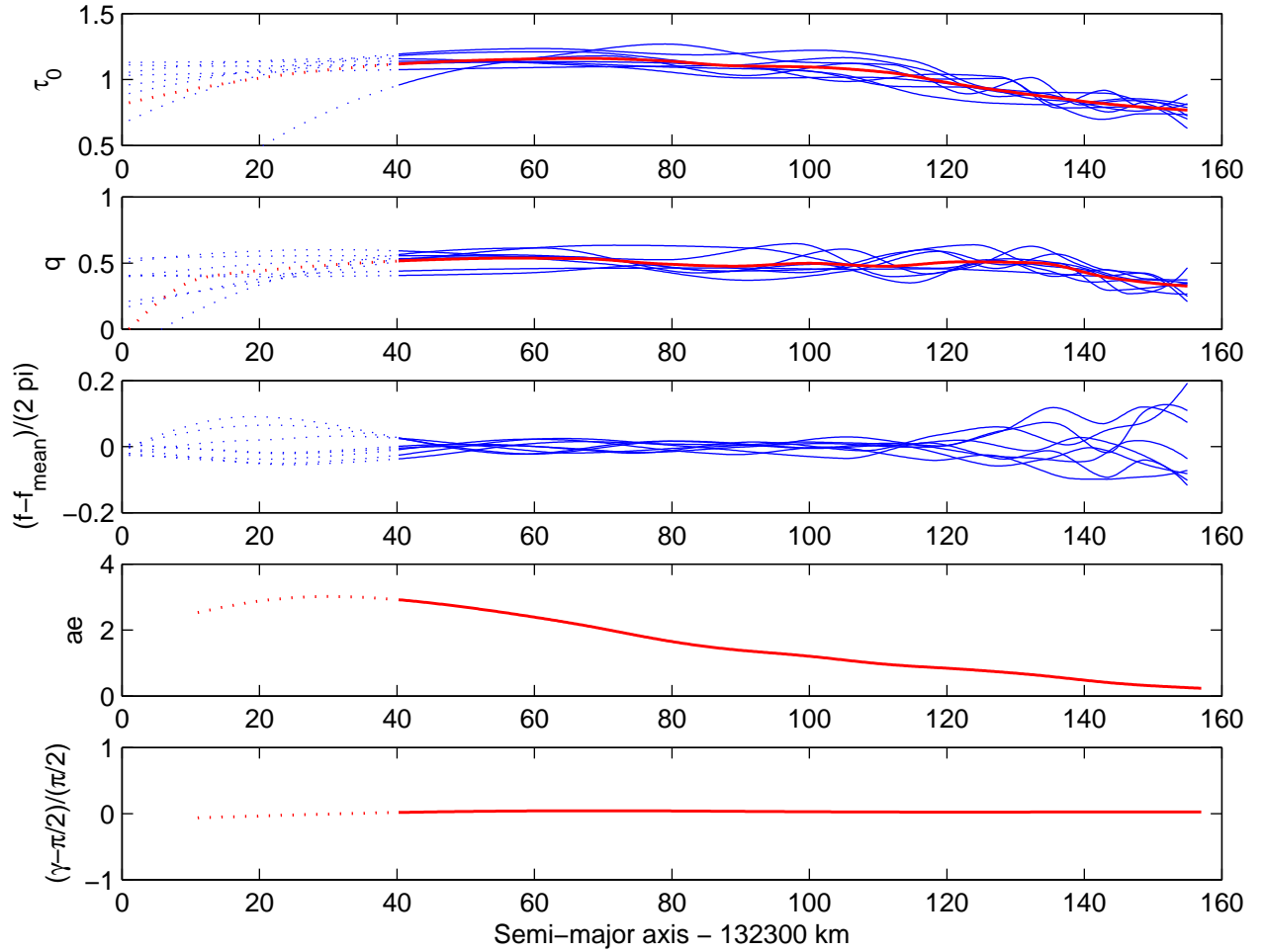


Figure 9: Retrieved kinematic parameters of the Mimas 5:3 density wave. The kinematic parameters obtained by considering the profiles independently from each other are shown in blue. The mean solution is displayed in red. The dotted lines refer to the region in which the parameters for at least one profile are extrapolated.

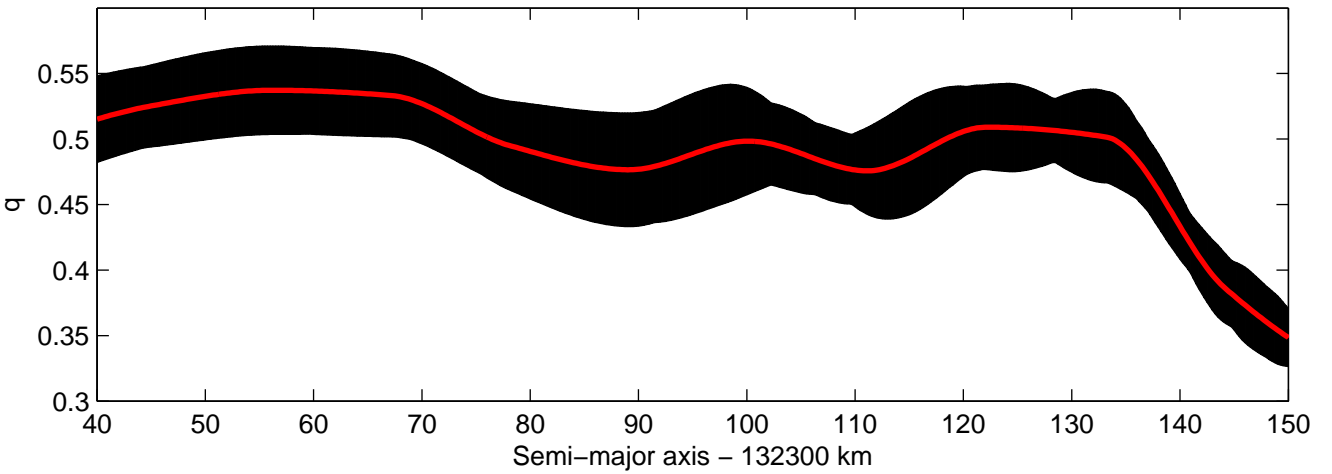
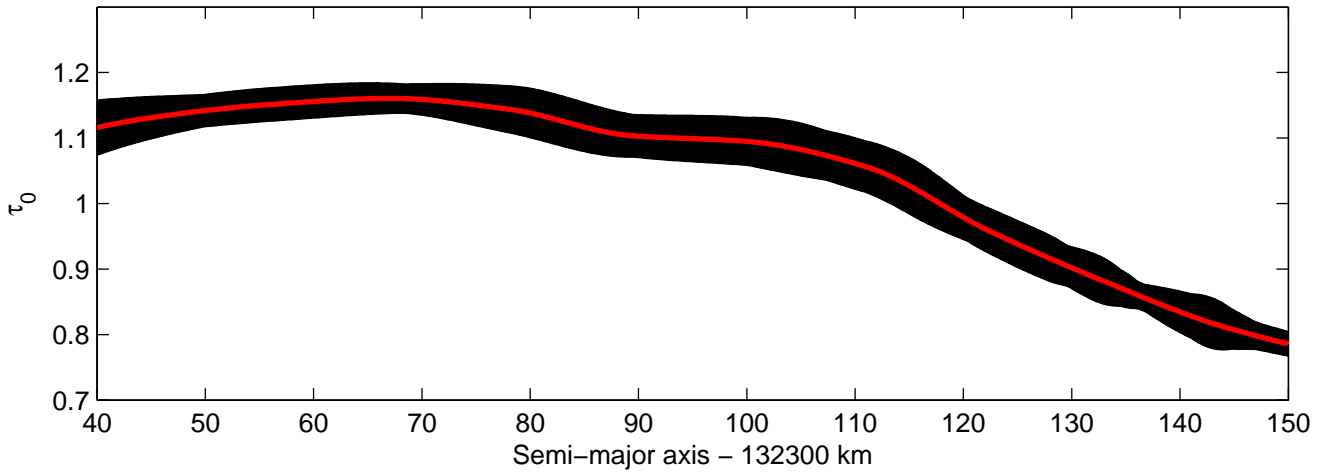


Figure 10: Mean solution (in red) for the background optical depth and the nonlinearity parameter surrounded by the error bars in black, for the Mimas 5:3 density wave.

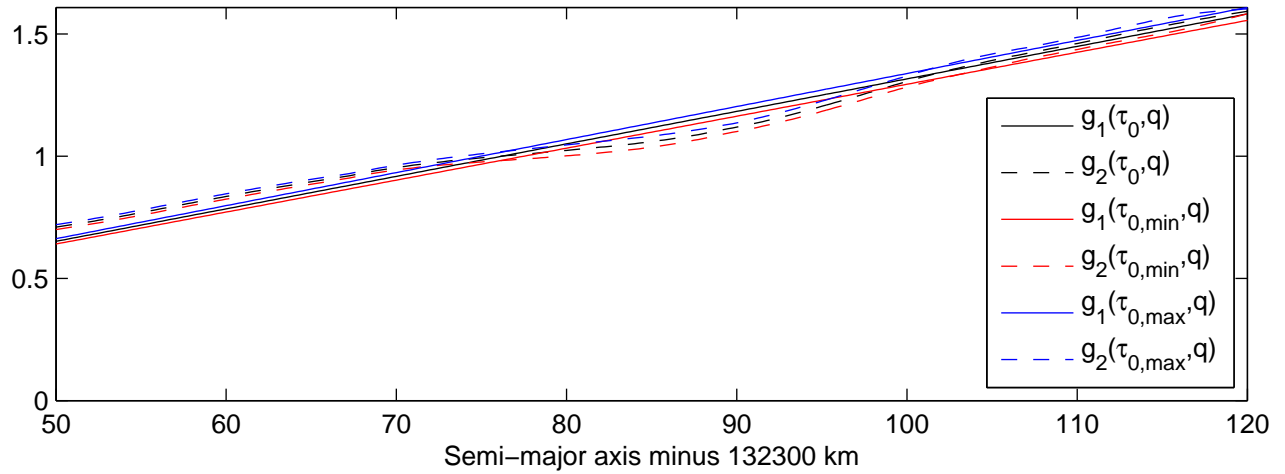
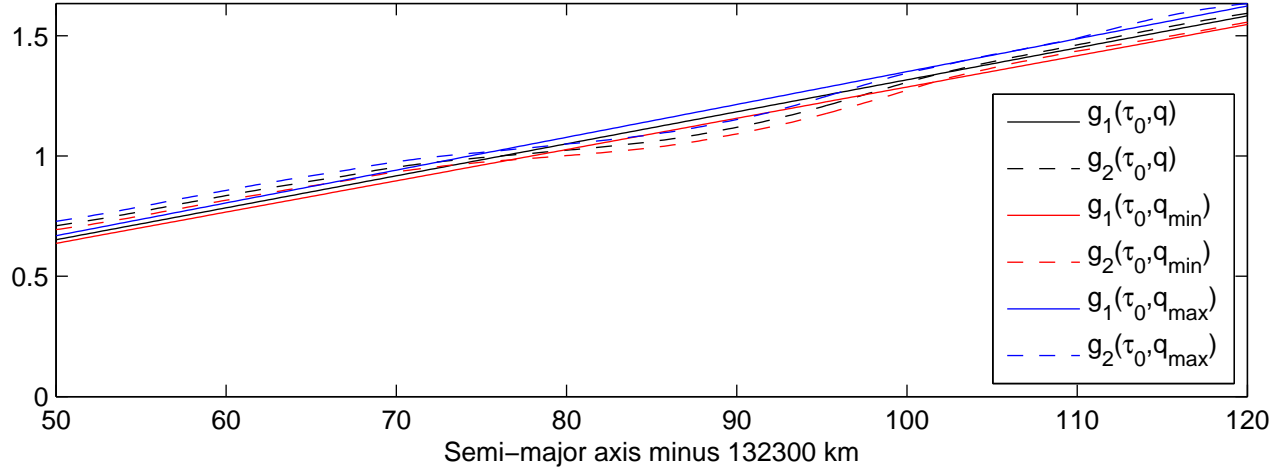


Figure 11: Functions g_1 and g_2 given by Eqs. (40) and (41) for various combination of τ_0 and q . Note that $\tau_{0,min}$, $\tau_{0,max}$, q_{min} , and q_{max} correspond to the values at the boundary of the error bar areas, and not to the minimum or maximum values of these variables obtained by treating the profiles independently.

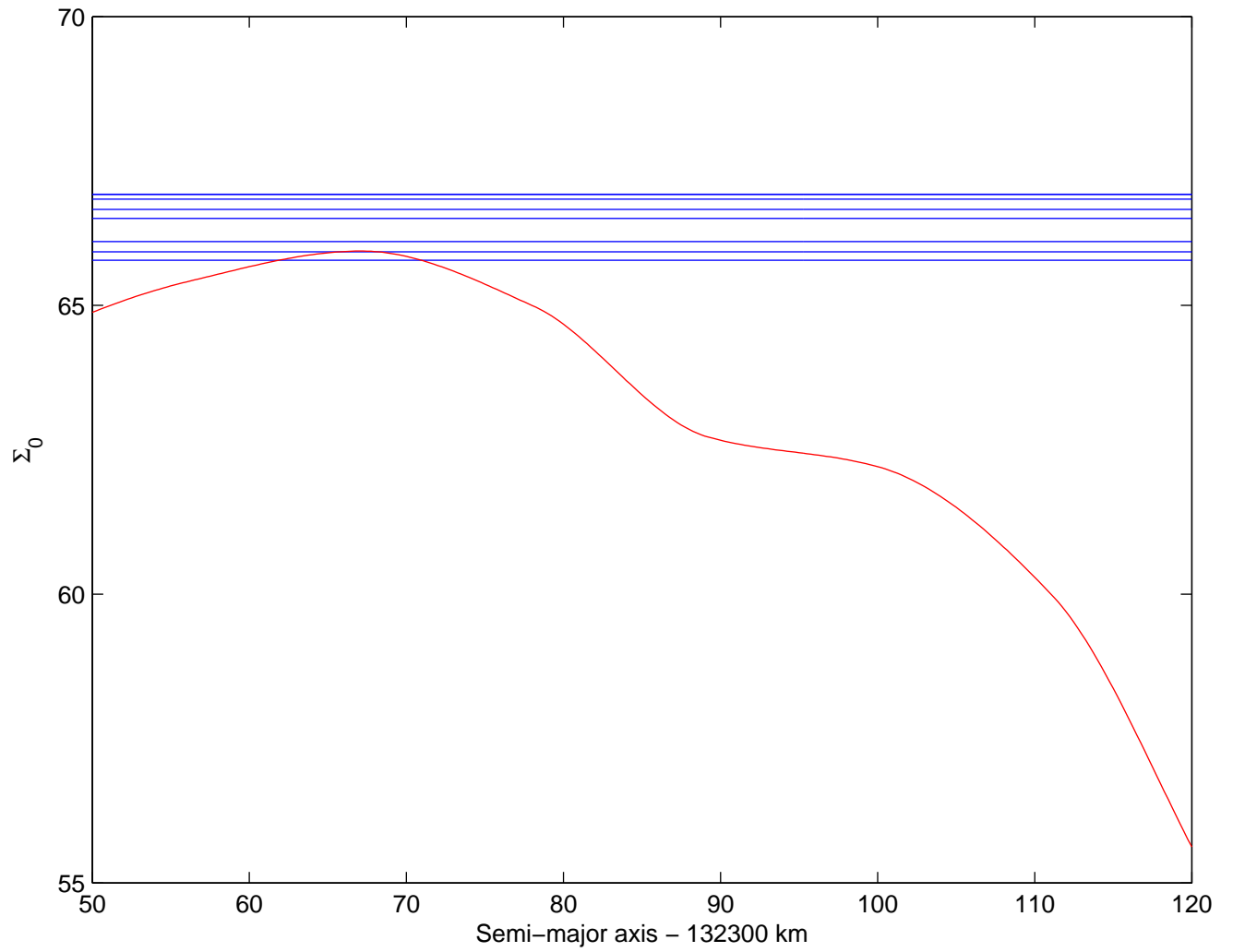


Figure 12: Surface density from the nonlinear theory (in red) and from the linear limit for each profile considered independently (in blue) for the Mimas density wave.

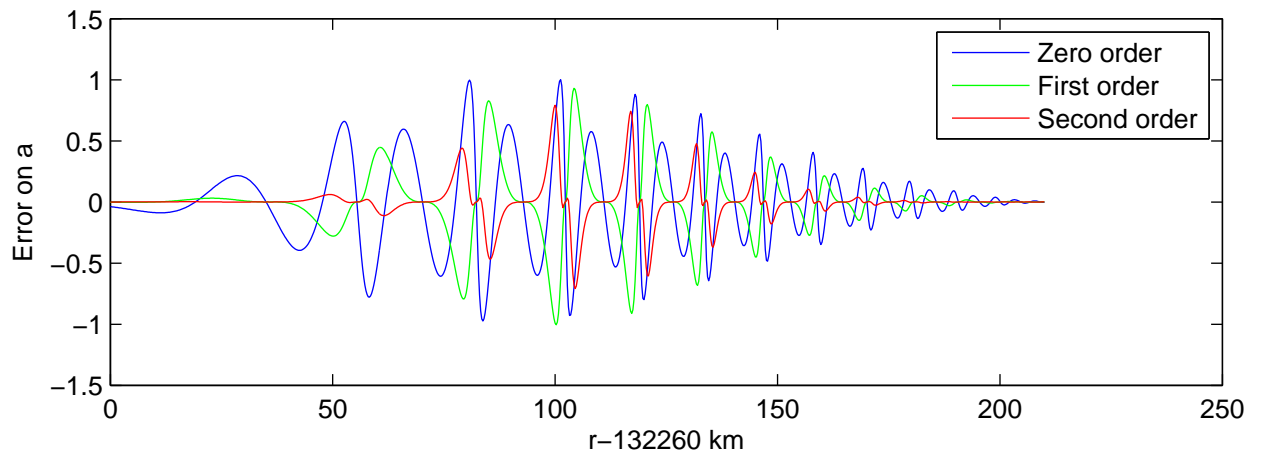


Figure 13: Error between the approximate $a(r)$ obtained when using the zeroth, first, and second order solutions and the actual $a(r)$.